JACS
JOURNAL OF THE AMERICAN CHEMICAL SOCIETY

ARTICLE

pubs.acs.org/JACS

A Step beyond the Feltham−Enemark Notation: Spectroscopic and Correlated *ab Initio* Computational Support for an Antiferromagnetically Coupled M(II)−$(NO)^-$ Description of Tp*M(NO) (M = Co, Ni)

Neil C. Tomson,[†] Mark R. Crimmin,[‡] Taras Petrenko,[†] Lauren E. Rosebrugh,[‡] Stephen Sproules,[†] W. Christopher Boyd,[‡] Robert G. Bergman,*[,‡] Serena DeBeer,*[,§] F. Dean Toste,*[,‡] and Karl Wieghardt*[,†]

[†]Max-Planck-Institut für Bioanorganische Chemie, Stiftstrasse 34-36, 45470 Mülheim an der Ruhr, Germany

[‡]Department of Chemistry, University of California, Berkeley, California, 94720, United States

[§]Department of Chemistry and Chemical Biology, Cornell University, Ithaca, New York 14853, United States

Supporting Information

ABSTRACT: Multiple spectroscopic and computational methods were used to characterize the ground-state electronic structure of the novel $\{CoNO\}^9$ species Tp*Co(NO) (Tp* = hydro-tris(3,5-Me_2-pyrazolyl)borate). The metric parameters about the metal center and the pre-edge region of the Co K-edge X-ray absorption spectrum were reproduced by density functional theory (DFT), providing a qualitative description of the Co−NO bonding interaction as a Co(II) ($S_{Co} = {}^3/_2$) metal center, antiferromagnetically coupled to a triplet NO^- anion ($S_{NO} = 1$), an interpretation of the electronic structure that was validated by *ab initio* multireference methods (CASSCF/MRCI). Electron paramagnetic resonance (EPR) spectroscopy revealed significant *g*-anisotropy in the $S = {}^1/_2$ ground state, but the linear-response DFT performed poorly at calculating the *g*-values. Instead, CASSCF/MRCI computational studies in conjunction with quasi-degenerate perturbation theory with respect to spin−orbit coupling were required for obtaining accurate modeling of the molecular *g*-tensor. The computational portion of this work was extended to the diamagnetic Ni analogue of the Co complex, Tp*Ni(NO), which was found to consist of a Ni(II) ($S_{Ni} = 1$) metal center antiferromagnetically coupled to an $S_{NO} = 1$ NO^-. The similarity between the Co and Ni complexes contrasts with the previously studied Cu analogues, for which a Cu(I) bound to NO^0 formulation has been described. This discrepancy will be discussed along with a comparison of the DFT and *ab initio* computational methods for their ability to predict various spectroscopic and molecular features.

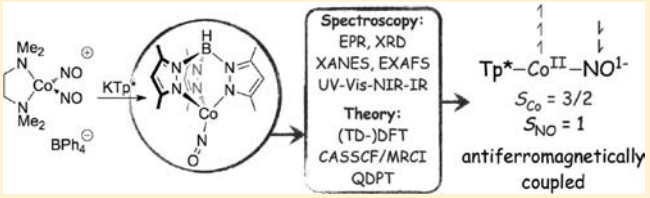

INTRODUCTION

Nitric oxide (NO) plays many roles in biological chemistry,[1] but the reactivity of NO is mediated primarily via interactions with metal-containing proteins through the complexation of first-row transition metals.[2−6] Considering the highly variable coordination chemistry of NO to these metals,[6] the ligand sphere and oxidation state of the metal center are critical factors for the protein environment to regulate, as subtle changes can result in dramatic differences in the M−NO interaction and, by extension, its reactivity.

Despite the biological importance of NO and its long history as a ligand in coordination chemistry,[7,8] descriptions of the bonding between NO and transition metals often fall to the purposefully ambiguous Feltham−Enemark notation:[9] $\{M(NO)_y\}^x$, where *y* is equal to the number of NO ligands and *x* is equal to the total number of electrons in the metal-d and NO-π^* orbitals. This ambiguity arises from the close relative energy of the NO-π^* orbitals compared to the d orbitals of first-row transition metals (especially those in biologically relevant oxidation states), which has made the accurate description of the bonding of NO to transition metal centers difficult.[6,10−14] Recent studies on a number of biologically relevant NO complexes by a combination of spectroscopic and computational methods have provided impetus for a bonding model in which NO can act as a redox-noninnocent ligand involving the antiferromagnetic coupling of metal-based and ligand-based electrons.[6] However, even within this more refined bonding model, the intrinsic ambiguity concerning oxidation and/or spin state assignments within such species has led to disagreements over the *most accurate* description of their ground-state electronic structures.

As an example of the ambiguity encountered in describing the electronic structure of such compounds, we consider the six-coordinate pseudo-octahedral $S = {}^3/_2$ $\{FeNO\}^7$ complex $(Me_3TACN)Fe(NO)(N_3)_2$ (Me_3TACN = *N*,*N*′,*N*″-trimethyl-1,4,7-triazacyclononane), which has sparked considerable debate

Received: June 29, 2011
Published: November 02, 2011

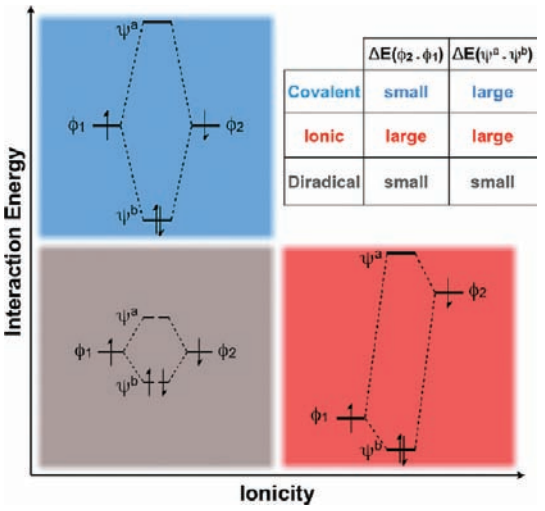

Figure 1. Plot relating the type of bonding (covalent, ionic, or diradical) to the relative energy (ionicity) and the overlap (interaction energy) of the two fragment orbitals φ_1 and φ_2.

in the literature. This complex is one of a host of biomimetic non-heme four-,[15,16] five-,[16−24] and six-[25−34] coordinate $\{FeNO\}^7$ complexes that have been studied extensively in recent years (in conjunction with heme $\{FeNO\}^7$ complexes[35]) for the insight they provide into biological NO processing. On the basis of electron paramagnetic resonance (EPR), X-ray absorption spectroscopy (XAS), and resonance Raman and magnetic circular dichroism spectroscopic studies, along with magnetic susceptibility measurements and density functional theory (DFT) calculations, Solomon and co-workers have argued that the bonding in $(Me_3TACN)Fe(NO)(N_3)_2$ may be assigned to an antiferromagnetically coupled Fe(III)/NO^- ($S_{Fe} = {}^5/_2$, $S_{NO} = 1$) formulation.[26,31] In contrast, Mössbauer spectroscopic studies, in combination with DFT calculations, led Oldfield and co-workers to propose an antiferromagnetically coupled Fe(II)/NO^0 ($S_{Fe} = 2$, $S_{NO} = {}^1/_2$) model.[33] Interpreting the same data, Rodriguez et al. have suggested that the unusual isomer shifts in the Mössbauer data suggest an oxidation state between ferric and ferrous and may be traced to a strong valence electron delocalization in the M−NO moiety rather than the separation of spin density onto metal and ligand fragments.[25,30] Thus, over a 15-year period, proposals spanning the range of reasonable valence bond pictures available to this complex have been put forth, but the chemical community has yet to arrive at a consensus view of the bonding for this species.

Ligand redox-non-innocence involving antiferromagnetic coupling can more generally be described by a classical singlet diradical bonding description and is thus a measure of both relative orbital energies (i.e., ionicity) and fragment orbital interaction energies (i.e., overlap), as illustrated in Figure 1. However, since a singlet diradical can originate *only* from low-ionicity fragment orbitals, difficulty can arise—as illustrated with the $(Me_3TACN)Fe(NO)(N_3)_2$ example—when investigating d_π-NO_{π^*} interactions as one attempts to distinguish a diradical bond (low-ionicity fragment orbitals with a *small* interaction energy) from a normal covalent π-bond (low-ionicity fragment orbitals with a *large* interaction energy). Various electron distributions—and thus physical oxidation states—may be obtained in either case, and the situations are distinguished only

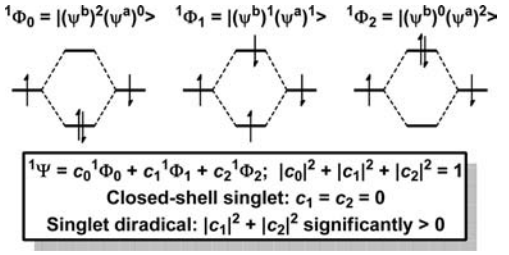

Figure 2. Representation of the contributions various singlet configurations make to the closed-shell and diradical bonding models. The magnitudes of c_1 and c_2 are inversely proportional to the interaction energy between the fragment orbitals.

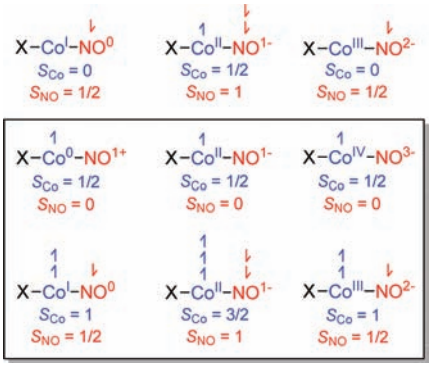

Figure 3. Limiting valence bond descriptions of $S_{tot} = {}^1/_2$ $\{CoNO\}^9$ complexes. The box encloses those with a residual Co-based spin system following the coupling of ligand-based and metal-based electrons. Single-headed arrows represent unpaired electrons, and X represents a monoanionic ligand.

by the degree of static ("left-right") correlation in the ground state (Figure 2), the presence of which may be simplistically interpreted as the spatial separation of the α- and β-components of the bonding orbital. In a valence bond picture, these magnetic orbitals may be construed as those involved in exchange coupling. The interactions of the d_π and NO_{π^*} orbitals within M−NO bonds are highly variable, depending on many factors, including the coordination number, coordination geometry, and metal-based Z_{eff}, but static correlation has been identified as a crucial component of M−NO (and related[36]) bonding, even for complexes with coordination numbers/geometries and oxidation states traditionally thought to be prohibitive toward such treatments.[24,37]

With an interest in contributing to the understanding of the interaction between late, first-row transition metals and NO, we herein report the synthesis, characterization, and ground-state electronic structure description of a simple, four-coordinate, mononitrosyl Co complex: Tp*Co(NO) (**1**, Tp* = hydrotris(3,5-dimethylpyrazolyl)borate). The three pyrazolyl donors provide a coordination sphere with relevance to biological systems, and the pseudotetrahedral coordination environment will be shown to have important consequences for the nature of the Co−N_{NO} bonding. The possible valence bond structures for this species are numerous (Figure 3), ranging from Co(0) to Co(IV) and including multiple spin states for both the ligand and the metal within many of the oxidation state assignments. Of particular importance, the electron count of this $\{CoNO\}^9$ species lends itself to spectroscopic investigation of the

ground-state electronic structure, creating an opportunity for the facile comparison of **1** to related first-row transition metal mononitrosyl species, including Co, Ni, and Cu complexes that have been reported in the literature. The most thoroughly studied of these are the Cu complexes originally reported by Tolman and co-workers, who suggested that the $\{CuNO\}^{11}$ species Tp′Cu(NO) (Tp′ = $Tp^{tBu,Ph}$, $Tp^{Ph,Ph}$, where $Tp^{R,R'}$ = hydro-tris(3-*R*,5-*R*′-pyrazolyl)borate) consist of a Cu(I)−$NO^{\bullet}$ ground state ($S_{Cu} = 0$, $S_{NO} = {}^1/_2$) on the basis of multiconfigurational *ab initio* calculations in combination with EPR and electronic absorption spectroscopy.[38,39] This work has been corroborated by Lehnert and co-workers, who reported additional spectroscopic and computational support for the Cu(I)−$NO^{\bullet}$ formulation.[40] However, while the analogous $\{NiNO\}^{10}$ tris(pyrazolyl)borate complexes Tp*Ni(NO) and $Tp^{Ph,Ph}$Ni(NO) are known, the bonding for these species has been described as either Ni(0)/NO^+ or Ni(IV)/NO^{3-},[41,42] neither of which is consistent with what one would expect for a nickel analogue of the more thoroughly studied copper complexes.

The work described herein has thus aimed to provide insight into the ground-state electronic structure of **1** through a combined spectroscopic and computational study. Our methods span X-ray diffraction (XRD), EPR, UV−vis−NIR, and X-ray absorption spectroscopies as well as DFT, time-dependent DFT (TD-DFT), complete active space self-consistent field (CASSCF), and multireference configuration interaction (MRCI) calculations. The resulting data are correlated between experiment and theory and thereby provide a detailed view of the interaction between the metal center and the nitrosyl ligand. The computational portion of the study has also been extended to include the known Ni analogue of **1**, Tp*Ni(NO) (**5**), as a means of highlighting trends in bonding from which those for related complexes may be extrapolated, and the Discussion Section will provide a comparison between **1**, **5**, and their Cu analogue, $Tp^{tBu,H}$Cu(NO). Finally, a comparison between the DFT and CASSCF/MRCI computational results, with respect to their ability to predict various spectroscopic features, will be discussed for evaluating the efficacy of single-determinant methods for modeling what are clearly multiconfigurational states.

EXPERIMENTAL SECTION

General Information. Unless otherwise indicated, operations were performed under anhydrous conditions and inert atmosphere employing standard Schlenk-line and glovebox techniques. All glassware was dried in an oven at 160 °C overnight or flame-dried prior to use. NMR spectra were acquired using Bruker AV-300, AVQ-400, AVB-400, and AV-500 spectrometers. Chemical shifts are reported as parts per million (ppm, δ), and ^{1}H and ^{13}C chemical shifts are referenced to the corresponding residual protic solvent resonance. Signal multiplicity and shape are reported using the following abbreviations: s, singlet; bs, broad singlet; d, doublet; t, triplet; q, quartet; m, complex multiplet. All low-resolution mass spectra (LR-MS) were recorded at the University of California, Berkeley Microanalytical Facility with electrospray ionization (ESI) or fast-atom bombardment (FAB) techniques in positive-ion mode. FAB mass spectra were recorded on a Micromass ZAB2-EQ magnetic sector instrument. Solvents were dried through a push-still system via passage through alumina. Cobalt(II) chloride was heated under vacuum (120 °C at 1×10^{-1} mbar) for 12 h prior to use. The cobalt complex [(TMEDA)Co(NO)$_2$][BPh$_4$] (TMEDA = *N*,*N*,*N*′,*N*′-tetramethylethylenediamine) was synthesized by a modification of the procedure reported by Caulton and co-workers.[43,44] Norbornene was distilled from calcum hydride and then degassed via successive freeze−pump−thaw cycles prior to use.

Table 1. Selected X-ray Acquisition Parameters for 1

molecular formula	$C_{15}H_{22}BCoN_7O$
formula weight (g mol^{-1})	386.14
crystal system	orthorhombic
space group	$Pmc2_1$
a (Å)	13.0809(18)
b (Å)	7.9962(11)
c (Å)	17.398(2)
α (deg)	90
β (deg)	90
γ (deg)	90
V (Å^3)	1819.8(4)
Z	4
μ (mm^{-1})	0.961
ρ (g cm^{-3})	1.409
θ range (°)	1.56−5.36
R_1,[a] wR_2[b] [$I > 2\sigma(I)$]	0.0395, 0.0740
R_1,[a] wR_2[b] (all data)	0.0591, 0.0827
measured/independent reflections/R_{int}	18 814/3424/0.0662

[a] $R_1 = \Sigma||F_o| - |F_c||/\Sigma F_o$. [b] $wR_2 = \{\Sigma[w(F_o^2 - F_c^2)^2]/\Sigma[w(F_o^2)^2]\}^{1/2}$, where $w = 1/\sigma^2(F_o^2) + (aP)^2 + bP$ and $P = (F_o^2 + 2F_c^2)/3$.

Syntheses. *Synthesis of Tp*CoNO (**1**).* In a glovebox, [(TMEDA)Co(NO)$_2$][BPh$_4$] (553 mg, 1 mmol, 1 equiv) was loaded into a Schlenk tube. Similarly, KTp* (336 mg, 1 mmol, 1 equiv) was weighed out and transferred to a separate Schlenk tube. The tubes were sealed, removed from the glovebox, and attached to a vacuum line. THF (20 mL) was transferred to each Schlenk tube via cannula under a positive pressure of nitrogen. The slurry of [(TMEDA)Co(NO)$_2$][BPh$_4$] was cooled to −78 °C with a dry ice/acetone bath, and the KTp* THF solution was then added via cannula. A slow color change to green was observed upon warming to room temperature. After an additional 30 min of stirring, the solvent was removed. The product could be isolated by extraction into hot toluene (20 mL); filtration and concentration of the resulting solution to approximately 5 mL, followed by hot recrystallization, provided **1** as a dark green solid (175 mg, 0.45 mmol, 45%). ^{1}H NMR (C_6D_6, 298 K, 400 MHz): δ −22.3 (9H, Me), 11.7 (3H, ArH) 28.5 (9H, Me). LR-MS (FAB, positive ion): 356 (100%, [M − NO]$^+$). IR (KBr disk, cm^{-1}): 2921, 2522, 1732, 1540, 1180. Elemental analysis calc for $C_{15}H_{22}BCoN_7O$: 46.66, C; 5.74, H; 25.39, N. Found: 46.17, C; 5.58, H; 24.20, N.

*Synthesis of **4** from **1**, Norbornene, and NO$_{(g)}$.* In a glovebox, **1** (41.0 mg, 0.106 mmol, 1 equiv) and norbornene (115 mg, 1.22 mmol, 11.5 equiv) were weighed into a Schlenk tube. The tube was sealed, removed from the glovebox, and attached to a vacuum line. Toluene (10 mL) was transferred into the Schlenk tube via cannula under a positive pressure of nitrogen. The reaction mixture was cooled to 0 °C and was placed under a partial vacuum, and then NO gas (1 atm) was introduced via the manifold. The reaction mixture was stirred at this temperature for 30 min, warmed to room temperature, and stirred for a further 30 min. After the reaction was complete, as determined by thin-layer chromatography, the system was flushed with argon, and the solvent was removed under reduced pressure. The crude solid was purified by silica gel chromatography to give **4** as a brown solid (31.6 mg, 0.62 mmol, 58%). ^{1}H NMR ($CDCl_3$, 400 MHz, 298 K): δ 1.19 (d, 1H, J = 10.4 Hz), 1.21−1.28 (m, 2H), 1.36−1.47 (m, 2H), 1.53 (d, 1H, J = 10.4 Hz), 1.89 (s, 9H, *Me*), 2.00 (m, 2H), 2.38 (s, 9H, *Me*), 3.05 (m, 2H, C*H*NO), 5.80 (s, 3H, *ArH*). ^{13}C NMR ($CDCl_3$, 100 MHz, 298 K): δ 12.6, 13.8, 26.4, 31.6, 37.6, 93.5, 107.4, 145.0, 150.4. IR (KBr disk, cm^{-1}): 3050, 2967, 2927, 2525, 1544, 1364, 1340. LR-MS (ESI, positive ion): 511 (100%, [M$^+$]), 416

(10%, $[M^+ - C_7H_{10}]$), 386 (20%, $[M^+ - (C_7H_{10} + NO)]$), 356 (95%, $[M^+ - (C_7H_{10} + 2NO)]$. UV−vis (nm, ε = mol^{-1} dm^3 cm^{-1}): 287 (22 000), 455 (10 000), 501 (sh, 9000). Elemental analysis calcd for $C_{22}H_{32}O_2BCoN_8$: 51.78, C; 6.32, H; 21.96, N. Found: 51.23, C; 6.26, H; 21.17, N.

Acquisition of X-ray Diffraction Data. The single-crystal XRD experiment on **1** (Table 1) was conducted at the UC Berkeley CheXray facility using a SMART APEX diffractometer equipped with a fine-focus sealed tube, a Mo Kα source, and a Bruker APEX-I CCD detector. A multiscan absorption correction was applied, and the structure was solved with SIR-97 and refined in SHELXL-97.

Acquisition of Electron Paramagnetic Resonance Data. X-band EPR data were recorded on a Bruker ESP 300 spectrometer and simulated with XSophe,[45] distributed by Bruker Biospin GmbH.

Acquisition of X-ray Absorption Spectra Data. Co K-edge XAS spectra were collected at the Stanford Synchrotron Radiation Lightsource (SSRL) at beamline 7-3 under ring conditions of 3 GeV and 200 mA. A Si(220) double-crystal monochromator was used for energy selection, and a Rh-coated mirror (set to an energy cutoff of 13 keV) was used for harmonic rejection. Incident and transmitted X-ray intensities were monitored using nitrogen-filled ionization chambers. X-ray absorption was measured in transmittance mode. During data collection, samples were maintained at a temperature of approximately 10 K using an Oxford Instruments liquid helium flow cryostat. Internal energy calibrations were performed by simultaneous measurement of the Co reference foil placed between the second and third ionization chambers with the inflection point assigned at 7709 eV. Data represent five scan averages. The data were calibrated and averaged using EXAFSPAK.[46] Pre-edge subtraction and splining were carried out using PYSPLINE.[47] A three-region cubic spline of order 2, 3, 3 was used to model the smooth background above the edge. Normalization of the data was achieved by subtraction of the spline and normalization of the post-edge region to 1. The resultant EXAFS was k^3-weighted to enhance the impact of high-k data. Theoretical EXAFS signals (k) were calculated using FEFF (version 7.0)[48] and fit to the data using EXAFSPAK. The nonstructural parameter E_0 was also allowed to vary but was restricted to a common value for every component in a given fit. The structural parameters varied during the refinements were the bond distance (R) and the bond variance (σ^2). The σ^2 is related to the Debye−Waller factor, which is a measure of thermal vibration, and to static disorder of the absorbers/scatterers. Coordination numbers were systematically varied in the course of the analysis, but they were not allowed to vary within a given fit.

Computational Procedures. All DFT and *ab initio* calculations were performed with the ORCA electronic structure package.[49] The DFT calculations were carried out at the OLYP[50] and B3LYP[51−53] levels of theory. The calculations were performed using def2 variants of the all-electron Gaussian basis sets of split-valence (def2-SVP) and triple-valence (def2-TZVP) quality as developed by the Ahlrichs group.[54] The basis set convergence of the computational results was checked using the triple-valence Gaussian basis def2-TZVPP augmented with the diffuse basis functions proposed by Dunning.[55] The calculations employed the resolution of identity (RI-J) algorithm for the computation of the Coulomb terms and the recently introduced "chain of spheres exchange" (COSX) algorithm for the calculation of the exchange terms.[56] For the fitting basis in the RI-J treatment, the 'def2' fit bases were used.[57] All calculations have been performed using an empirical van der Waals correction to the DFT energy.[58−60]

The SCF calculations were tightly converged (1×10^{-8} E_h in energy, 1×10^{-7} E_h in the density change, and 5×10^{-7} in the maximum element of the DIIS error vector). In all cases the geometries were considered converged after (i) the energy change was $<1 \times 10^{-6}$ E_h, (ii) the gradient norm and maximum gradient element were smaller than 3×10^{-4} and 1×10^{-4} E_h $bohr^{-1}$, respectively, and (iii) the root-mean-square and maximum displacements of all atoms were smaller than 6×10^{-4} and 1×10^{-3} Bohr, respectively. All geometry optimization calculations were carried out on redundant internal coordinates without imposing symmetry constraints. Canonical, unrestricted corresponding orbitals (UCOs),[61] quasi-restricted orbitals (QROs)[62] (electron density isosurface threshold = 0.05), and spin density plots (electron density isosurface threshold = 0.005) were generated with the program Molekel, v4.3.[63] We have used the general abbreviation BS(m,n) to denote a broken-symmetry (BS) DFT calculation with m unpaired or partially paired spin-up electrons and n partially paired spin-down electrons as the two interacting fragments.[64]

TD-DFT calculations using the B3LYP functional were performed to predict the transitions in the pre-edge region of the Co K-edge XAS spectra.[65,66] The basis sets were chosen to match the basis sets used for the single-point ground-state calculations, except for Co, for which the CP(PPP) basis set[67] was used. The obtained Co K-edge transition energies were shifted by a constant value of 165.1 eV to ease comparison with the experimental spectra.

On the phenomenological level, the exchange coupling was treated using the well-known Heisenberg−Dirac−van Vleck (HDvV) Hamiltonian:

$$H_{HDvV} = -2J\hat{S}_A \cdot \hat{S}_B \quad (1)$$

For predicting the exchange coupling constant J, we have employed DFT and wave function-based methodologies. The first approach is realized using the BS method of Noodleman,[68,69] which allows one to treat systems with unpaired electrons within the restriction of a single spin-unrestricted determinant. Having obtained spin-unrestricted solutions for the determinants of maximum spin, using $M_S = S_A + S_B$, and BS spin, using $M_S = |S_A - S_B|$, the following definitions of J were employed.

Noodleman's equation, which is valid in the weak coupling limit, reads[68−70]

$$J^1 = -\frac{E_{HS} - E_{BS}}{(S_A + S_B)^2} \quad (2)$$

where E_{HS} and E_{BS} are the energies of the high-spin (HS) and BS determinants, respectively. The following definition of J, given by Bencini,[71] is suitable in the strong coupling limit:

$$J^2 = -\frac{E_{HS} - E_{BS}}{(S_A + S_B)(S_A + S_B + 1)} \quad (3)$$

We have also used an expression for J which is valid over the whole coupling strength regime, as discussed by Yamaguchi and co-workers:[72,73]

$$J^3 = -\frac{E_{HS} - E_{BS}}{\langle \hat{S}^2 \rangle_{HS} - \langle \hat{S}^2 \rangle_{BS}} \quad (4)$$

The final spin energy ladder was computed by direct diagonalization of the HDvV Hamiltonian.

Alternatively, since the case of exchange coupling can be regarded as extremely weak chemical bonding, thus implying significant multireference character in the system, we have also applied wave function-based multireference correlation treatments. MRCI calculations were done employing the state-averaged complete active space self-consistent field (SA-CASSCF) method for the calculation of the zeroth-order wave function. In individually selecting MR-CI calculations, a test configuration was kept if its perturbation energy $H_{I0}^2/\Delta E$ was larger than a certain threshold T_{sel} (H_{I0} is the CI matrix element between the test configuration and muticonfigurational zeroth-order wave function, and ΔE is the energy difference calculated with the Möller−Plesset (MP) zeroth-order Hamiltonian). The values reported in the main body of the paper were obtained with $T_{sel} = 10^{-8}$ E_h, which led to well-converged results. The energetic effect of unselected configuration state functions (CSFs)

Scheme 1. Synthesis of Tp*Co(NO) (1)

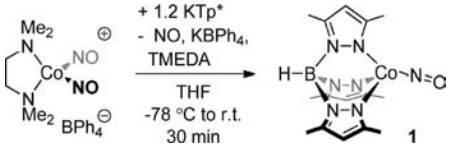

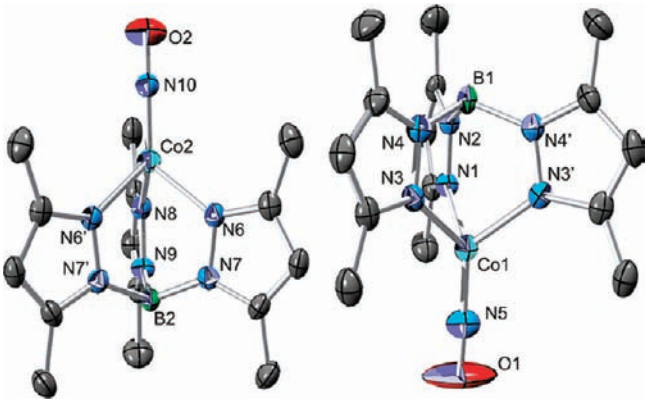

Figure 4. ORTEP representation of the symmetry-expanded asymmetric unit of **1**, showing the two independent molecules present in the crystal lattice. Thermal ellipsoids at 50% probability level; hydrogen atoms removed for clarity. Selected bond lengths (Å) and bond angles (°): Co(1)−N(5) 1.625(5), N(5)−O(1) 1.161(6), Co(1)−N(1) 2.010(4), Co(1)−N(3) 2.009(3), Co(1)−N(5)−O(1) 173.5(6), B(1)−Co(1)−N(5) 173.44, Co(2)−N(10) 1.628(5), N(10)−O(2) 1.167(6), Co(2)−N(6) 1.994(3), Co(2)−N(8) 2.013(5), Co(2)−N(10)−O(2) 175.5(6), B(2)−Co(2)−N(10) 175.86.

was estimated by second-order Rayleigh−Schrödinger theory using MP partitioning. We have explored the difference dedicated CI (MR-DDCI3) approach of Caballol, Malrieu, and co-workers[74] as well as Neese's SORCI method.[75]

Molecular *g*-tensors were calculated using the Gerloch−McMeeking formalism.[76,77] It can be shown that the Zeeman interaction in the basis of the ground-state Kramers pair $|\Phi\rangle$ and $|\bar{\Phi}\rangle$ can be modeled by the Zeeman spin-Hamiltonian in the basis of the pseudospin functions $|+\rangle$ and $|-\rangle$. The corresponding *g*-tensor is calculated from the so-called **G**-matrix:

$$G_{kl} = 2 \sum_{I,J=\Phi,\bar{\Phi}} \langle I|\hat{L}_k + g_e\hat{S}_k|J\rangle\langle J|\hat{L}_l + g_e\hat{S}_l|I\rangle \quad (5)$$

where $\hat{\mathbf{L}}$ and $\hat{\mathbf{S}}$ are the orbital and spin angular momentum operators, respectively. The *g*-factors are calculated as the positive square roots of the three eigenvalues of **G**.

The ground-state Kramers pair is obtained using an infinite-order solution (quasi-degenerate perturbation theory, QDPT[78]) with respect to spin−orbit coupling (SOC) in the basis of a finite number of scalar-relativistic eigenstates of the Born−Oppenheimer (BO) Hamiltonian $\hat{H}_{BO}$. In this approach, the Hamiltonian,

$$\hat{H} = \hat{H}_{BO} + \hat{H}_{SOMF} \quad (6)$$

which involves the SOC mean-field Hamiltonian of the form[79]

$$\hat{H}_{SOMF} = \sum_i \hat{h}^{SOC}(i)\hat{s}(i) \quad (7)$$

is diagonalized in the basis of solutions to the BO Hamiltonian, which were obtained from SA-CASSCF or MRCI calculations.

Scheme 2. Generation of Tp*Co(NO)$_2$ (3) from 1 and NO and Subsequent Alkene Trapping To Form 4

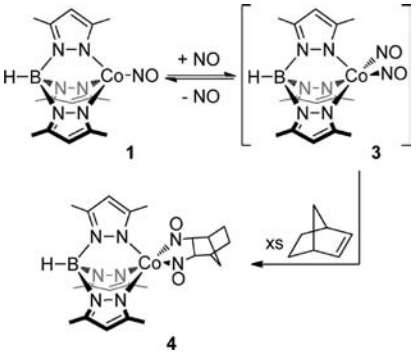

RESULTS AND ANALYSIS

Synthesis and Reactivity of Tp*Co(NO). The reaction of $[(TMEDA)Co(NO)_2][BPh_4]$[43,44] with KTp* in THF at −78 °C followed by warming to room temperature yielded Tp*Co(NO) (**1**, Scheme 1)—a green compound that could be isolated by recrystallization from toluene in moderate but reproducible yields of 30−45%. Compound **1** exhibits a single NO stretching frequency at 1732 cm^{-1}, almost identical to the value 1736 cm^{-1} reported for Tp^{tBu,Me}Co(NO) (**2**).[80] The paramagnetic nature of **1** was immediately apparent from 1-D ^{1}H NMR spectroscopic data, with resonances occurring at δ −22.3 (s, 9H), 11.7 (s, 3H), and 28.5 (s, 9H) ppm.

Compound **1** crystallizes in the orthorhombic space group $Pmc2_1$, with two molecules present in the asymmetric unit (Figure 4). Metrical parameters between the two molecules within the unit cell of **1** differed little. Although **2** provides a useful point of comparison, the crystallographic C_3 symmetry imposed by the complex's rhombohedral space group ($R3m$) precludes determination of subtle structural features that deviate from the crystallographic C_3-axis. Indeed, a comparison of the Co−N bond lengths (**1**, 2.009(3), 2.010(4), 1.625(5) Å; **2**, 2.030(4), 1.671(7) Å), the N−O bond length (**1**, 1.161(6) Å; **2**, 1.071(9) Å), and the Co−N−O (**1**, 173.5(6) °; **2**, 180°) and B−Co−NO bond angles (**1**, 173.5°; **2**, 180°) leads to the conclusion that the short N−O bond length and the idealized Co−N−O bond angle found in the solid-state structure of **2** are due to disorder about the three-fold axis.[80] This observation is further underpinned by DFT calculations on **1** (*vide infra*) and the reported average N−O bond length of 1.159 Å cited for a range of metal nitrosyl complexes.[9]

As alluded to in our previous work,[81] compound **1** readily undergoes reaction with NO. Treating Tp*CoNO with excess NO in d_8-toluene results in an equilibrium mixture of **1** + NO and Tp*Co(NO)$_2$ (**3**) as observed by ^{1}H NMR spectroscopy (Scheme 2). The chemical shift values were concentration-weighted averages of those for **1** and the diamagnetic $\{Co(NO)_2\}^{10}$ complex **3**, suggesting a fast exchange process at room temperature. Theopold and co-workers have reported a similar dynamic equilibrium: under an atmosphere of CO, Tp^{iPr,Me}Co(CO) reversibly forms Tp^{iPr,Me}Co(CO)$_2$.[82]

Evidence for the composition of **3** was provided by a trapping experiment with an alkene. Consistent with studies upon the ligand-based reaction chemistry of CpCo(NO)$_2$, a similar five-coordinate cobalt dinitrosyl complex,[83−90] performing the reaction

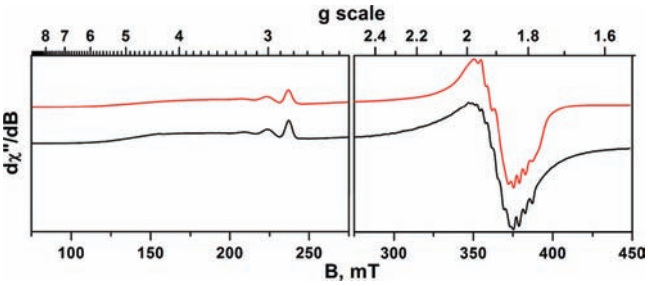

Figure 5. Selected portions of the X-band EPR spectra of **1** in 1:1 dichloromethane:toluene at 10 K (left) and in dichloromethane at 20 K (right). Conditions: (left) frequency, 9.419 GHz; power, 0.63 mW; modulation, 1.0 mT; (right) frequency, 9.621 GHz; power, 0.10 mW; modulation, 0.7 mT. Simulated spectrum in red (top); experimental spectrum in black (bottom). Data collection in different solvent systems allowed for the fortuitous resolution of hyperfine splitting in complementary portions of the spectra. The more finely resolved portions of the spectra are shown here, and the complete spectra from each solvent system are given in the Supporting Information.

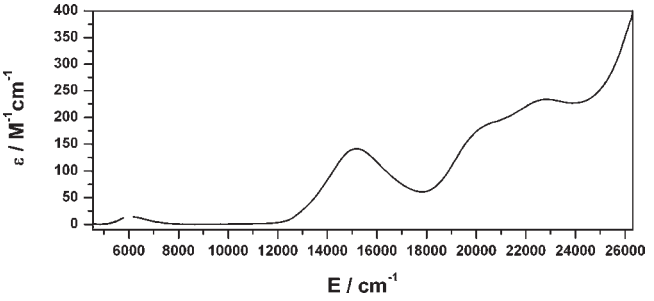

Figure 6. Vis−NIR spectrum of **1** in CH_2Cl_2 at 298 K.

of **1** with NO in the presence of an excess of norbornene allowed for the isolation of the dinitrosoalkane complex **4** in 53% yield (Scheme 2). As reported previously,[81] addition of norbornene to the reaction conditions used for synthesizing **1** provided **4** in 65% yield. This latter experiment provides further support that the reaction between **1** and NO to form **3** is reversible.

Spectroscopic Characterization of Tp*Co(NO). X-band EPR spectra of **1** collected between 10 and 20 K provide clear evidence for an $S_{tot} = {}^1/_2$ system,[91] and the significant *g*-anisotropy (g_x = 1.814, g_y = 1.910, g_z = 3.505) and large hyperfine coupling strongly suggest a Co-centered spin. The g_z component was modeled with $A_z\{^{59}Co\} = 213.0 \times 10^{-4}$ cm^{-1}, and the g_x and g_y components were fit with $A_x\{^{59}Co\} = 28.2 \times 10^{-4}$ cm^{-1} and $A_y\{^{59}Co\} = 29.0 \times 10^{-4}$ cm^{-1}, respectively, using data collected in different solvent systems (Figure 5, Supporting Information). Consistent with the unusual bonding of NO to transition metal centers, these data contrast dramatically with those recently reported for a number of isoelectronic d^7 cobalt(II) tris(pyrazolyl)borate complexes of the form $Tp^{tBu,Me}$CoX (X = NCS, NCO, N_3, Cl). The latter complexes have been shown to be $S_{tot} = {}^3/_2$ species by EPR spectroscopy.[92]

The vis−NIR spectrum of **1** collected in dichloromethane revealed four main features in the range of 5000−25000 cm^{-1} (Figure 6). The lowest energy feature at 6173 cm^{-1} (ε = 14 M^{-1} cm^{-1}) was extremely weak in intensity, but the distribution profile precluded a vibronic origin of the signal. The higher energy features fall in the energy and molar absorptivity ranges

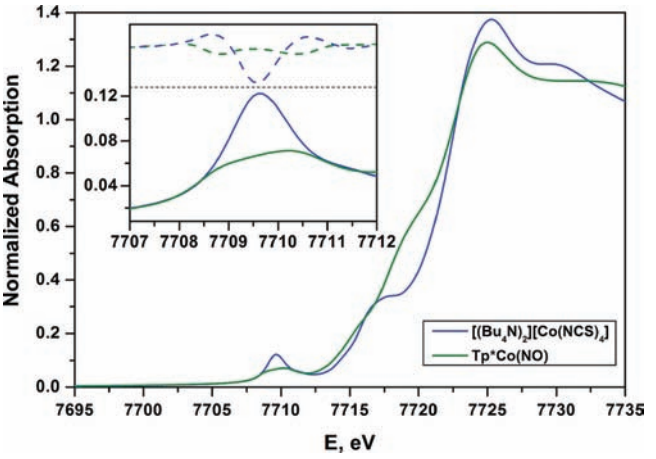

Figure 7. Comparison of the normalized Co K-edge XAS spectra of **1** (green) and $[(Bu_4N)_2][Co(NCS)_4]$ (blue). The inset shows an expansion of the initial pre-edge regions of the experimental data along with a plot of the second derivatives of the two spectra (dashed lines).

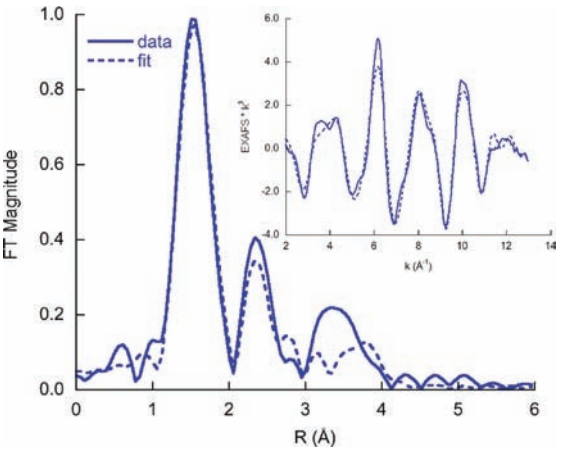

Figure 8. Non-phase-shift-corrected Fourier transform for **1** (solid line) and the corresponding fit (dashed line). The k^3-weighted EXAFS and the fit are given in the inset.

traditionally assigned to d−d transitions, with an isolated absorption band at 15 198 cm^{-1} (ε = 141 M^{-1} cm^{-1}) along with two shoulders at 20 284 cm^{-1} (ε = 183 M^{-1} cm^{-1}) and 22 831 cm^{-1} (ε = 234 M^{-1} cm^{-1}).

Co K-edge XAS of **1** and $[(Et_4N)_2][Co(NCS)_4]$ provided experimental data on the physical oxidation state of Co in **1**. The latter complex was chosen to serve as an oxidation-state standard for Co(II) in an N_4-pseudotetrahedral environment. The initial pre-edge feature for $[Co(NCS)_4]^{2-}$, which corresponds to the 1s→3d transitions into the t_2 orbitals, was observed at 7709.6 eV with a full-width half-maximum (fwhm) of ca. 1.5 eV. The initial pre-edge feature of **1** was observed at 7708.8 eV, with a closely spaced second feature at 7710.3 eV (Figure 7). The 0.8 eV lower energy initial pre-edge feature of **1** compared to that of $[Co(NCS)_4]^{2-}$ precludes formal Co(0), Co(III), or Co(IV) physical oxidation state assignments to the metal center in **1**, since a shift of ca. 1.0 eV per unit change in oxidation state is common when comparing molecules with similar ligand field environments. In combination with the EPR study, these data

Table 2. EXAFS Fit Parameters for 1

component	R (Å)	σ^2 (Å^2)	ΔE_0 (eV)	error[a]
1 Co−N	1.65	0.0070	−1.1	0.26
3 Co−N	2.02	0.0036		
4 Co−C/N/O	2.87	0.0043		
4 Co−C	4.24	0.0022		

[a] Error is given by $\Sigma[(\chi_{obsd} - \chi_{calcd})^2 k^6]/\Sigma[\chi_{obsd}{}^2 k^6]$.

Table 3. Experimental and Calculated Metric Parameters for Complexes 1, 2, and TpCo(NO) (1′, See Text)

	1[a]	2[a]	1[b]	1[c]	1′[b]
Co−NO (Å)	1.625(5)	1.671(7)	1.7166	1.6445	1.7160
N−O (Å)	1.161(6)	1.071(9)	1.1813	1.1823	1.1780
Co−N_{Tp^*} (Å)	2.009(3)	2.030(4)	2.0444	2.0205	2.0579
	2.009(3)	2.030(4)	2.0623	2.0210	2.0767
	2.010(4)	2.030(4)	2.0624	2.0449	2.0774
Co−N−O (°)	173.5(6)	180	163.5	160.0	165.2
α-angle[d] (°)	6.5	0	19.0	19.3	15.0

[a] XRD experimental data. [b] B3LYP-optimized data. [c] OLYP-optimized data. [d] Defined as 180° − ∠B−Co−NO.

thus imply either a Co(I)−$NO^{\bullet}$ (S_{Co} = 1, S_{NO} = $^1/_2$) or a Co(II)−NO^- (S_{Co} = $^3/_2[^1/_2]$, S_{NO} = 1[0]) ground-state configuration (Figure 3).

Due to the difficulties in modeling the disorder in the X-ray structure, EXAFS data were also obtained for **1**. The best fit to the EXAFS data together with the corresponding Fourier transforms are given in Figure 8. The data are best fit by one Co−N at 1.65 Å and three Co−N interactions at 2.02 Å, in good agreement with the crystal structure. Additional contributions due to multiple scattering from both the Tp* and NO ligands are required to fit the outer shells of the FT, as indicated in Table 2. Due to the overlapping multiple scattering contributions from the NO and the pyrazole rings, the Co−NO angle could not be unambiguously determined from the EXAFS data. We also note the σ^2 value, which at 10 K primarily reflects static disorder in metal−ligand bonds, is rather large for the Co−N interaction (0.007 Å^2). This likely reflects the disorder in this vector, which was also observed crystallographically.

DFT Calculations on Tp*Co(NO). *Geometry Optimization.* The geometry of **1** was optimized using both the B3LYP and OLYP functionals. These choices were made to facilitate comparison of our work with (i) the majority of transition metal DFT calculations being performed today (B3LYP) and (ii) a growing subset of metal nitrosyl complexes which seem to be well described by the OLYP GGA functional.[13,21,22,24,93,94] In both cases the metric parameters were well reproduced (Table 3), with the main exception being the differences in the Co−NO bond distances and B−Co−NO angles; these parameters deviate from the crystallographic data due to disorder in the crystal lattice, as evidenced by the large thermal parameters for the oxygen of the nitrosyl ligand. The optimized coordinates from the B3LYP (OLYP) calculations indicate an α-angle (α = 180° − ∠B−Co−NO) of 18.6° (19.3°) and a Co−NO distance of 1.7166 Å (1.6445 Å). Simple trigonometric analyses on these data reveal that crystallographically imposed C_3 symmetry would result in Co−NO bond lengths of 1.6272 Å (1.5521 Å). Particularly for the B3LYP calculation, this result provides good qualitative agreement with the experimentally determined values. Scans of the potential energy surfaces concerning changes in either d(Co−N_{NO}) or ∠(B−Co−N_{NO}) suggest that very little energy is associated with these deformations (see Supporting Information).

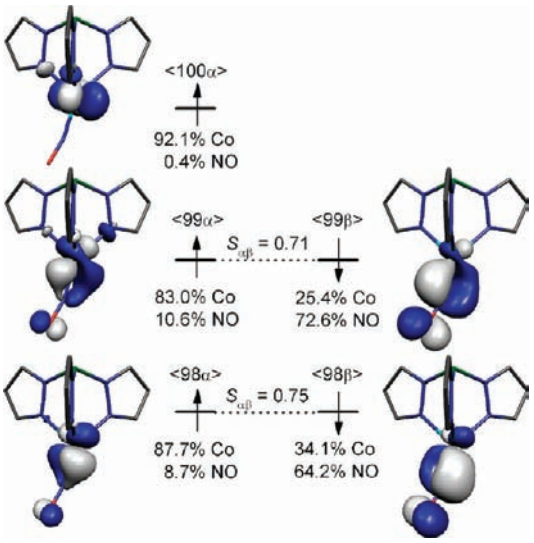

Figure 9. Calculated frontier UCOs for **1** from a B3LYP geometry optimization calculation. The methyl groups and hydrogens were removed for clarity. $S_{\alpha\beta}$ refers to the degree of spatial overlap between the magnetic orbitals.

Ground-State Electronic Structure. For all DFT-optimized geometries, the electronic structure resulting from UKS-B3LYP single-point energy calculations, followed by analysis using the UCO transformation,[61] is that of a highly spin-polarized ground state, comprising an S = $^3/_2$ Co(II) ion antiferromagnetically coupled to an S = 1 NO^- anion. The same solution has been obtained using the BS methodology, via exchange of the α and β blocks of spin density on NO following convergence on the high-spin (S = $^5/_2$) wave function (FlipSpin keyword in ORCA, resulting solution denoted as BS(3,2)). The spin-contamination associated with this solution ($\langle S^2 \rangle$ = 1.696, versus the ideal value of $S(S+1)$ = 0.750), is indicative of a multideterminant ground state. In general, weak chemical bonding, which is implied in the presence of exchange-coupled fragments, can be properly treated by *ab initio* multireference methods, but the BS methodology[68,69] represents an alternative approach in which the problem of calculating J is solved using single-reference SCF methods. In principle, it is possible to obtain an infinitely large number of BS solutions. Typically, the solution that corresponds to the expected valence bond picture is chosen, and/or the lowest energy solution is selected from among several trial BS solutions; below we analyze the BS(3,2) solution. The corresponding spin energy ladder and the valence bond-like description of the electronic structure, as derived from the BS(3,2) DFT calculations, will be validated by comparison with more rigorous MRCI calculations (vide infra).

Taking the results from the B3LYP-optimized coordinates as an example, we find a Co-based SOMO (92.1% Co) with a negligible (<1%) contribution from the nitrosyl ligand (Figure 9), consistent with the signal observed by EPR spectroscopy (Figure 5). The α-spin components of the antiferromagnetically coupled orbitals comprise a metal-based e set (here d_{xz} and d_{yz};

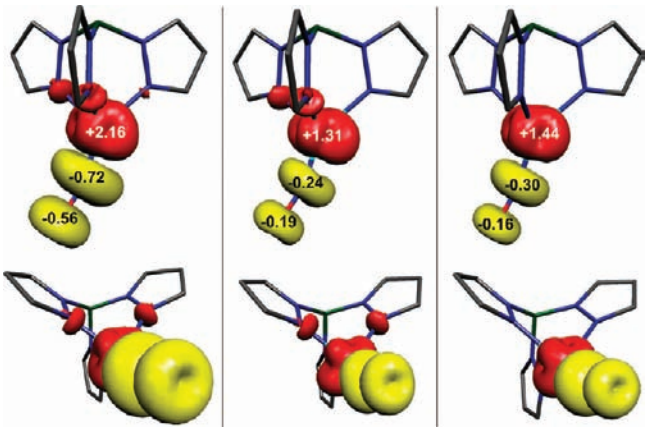

Figure 10. (Left, middle) Spin density plots with numerically annotated Mulliken spin densities for Tp*Co(NO) from BS(3,2) single-point energy calculations using the B3LYP (left) and OLYP (middle) functionals on the UKS-B3LYP and UKS-OLYP optimized coordinates, respectively. The methyl groups and the hydrogens were removed for clarity. (Right) Spin density plot with numerically annotated Mulliken spin densities for TpCo(NO) from a CASSCF(5,5) single-point energy calculation.

the *z*-axis lies along the Co−B vector, and the molecular mirror plane describes the *xz*-plane), which rehybridize from those of a non-π-bonding L_4M tetrahedral field to allow for overlap with the NO-π^* orbitals. This rehybridization accounts for the uptake of an antibonding interaction within the SOMO between the d_{xy} and a linear combination of two Tp*-based sp^2-σ-donor orbitals. Together, the metal-centered SOMO and the two α-spin components of the antiferromagnetically coupled orbitals—all of which are significantly metal-centered (83.0−92.1% Co)—account for the three spin-up electrons of the high-spin Co(II) ion. By comparison, the two β-spin components of the antiferromagnetically coupled orbitals display significant NO-π^* character (64.2−72.6%) and represent the two ferromagnetically coupled spins responsible for the $S = 1$ NO^- formulation of the ligand.

The similarity in the calculated exchange coupling parameters J^1 (-2600 cm^{-1}) and J^3 (-2299 cm^{-1}) from this UKS-B3LYP calculation is consistent with the bonding of interest being in the weak-overlap regime,[72] as manifested by the differing spatial distributions of the α- and β-spin components of the antiferromagnetically coupled orbitals. This spatial separation leads to significant spin density beyond that which would correspond to a single unpaired electron in the SOMO, thus resulting in 2.16 α-spin electrons on Co and 1.29 β-spin electrons on NO (Figure 10). Spin polarization of the Tp*−N σ-bonding orbitals accounts for the majority of the remaining spin density in the molecule.

OLYP single-point energy calculations on the coordinates obtained from either B3LYP or OLYP geometry optimization calculations suggest much greater overlap in the antiferromagnetically coupled orbitals. Again, the results from either geometry are qualitatively identical; here we discuss the single-point energy calculation on the OLYP-optimized coordinates to illustrate the limits of spatial overlap and covalency in this system. The overlap integrals in this case are close to unity ($S_{\alpha\beta}$(HOMO−1) = 0.98, $S_{\alpha\beta}$(HOMO) = 0.96), resulting in a decrease in the spatial separation of the magnetic orbital components. However, the spin density values, while decreased in magnitude (+1.31 on Co and −0.43 on NO), retain the same spatial character as those of the B3LYP single-point energy calculations (roughly spherical about Co and cylindrical about NO, Figure 10). The greater overlap of the magnetic orbitals is accompanied by larger exchange coupling parameters (Table 4), where crossover into the strong-overlap regime is manifested by agreement between the J^2 and J^3 parameters (-3041 and -3372 cm^{-1}, respectively).[72,73] Thus, the best agreements between the B3LYP- and OLYP-determined *J*-values, and, by extension, the state energy differences ($\Delta E(^4\Gamma - {}^2\Gamma) = -3J$; $\Delta E(^6\Gamma - {}^2\Gamma) = -8J$), are J^1(B3LYP), J^2(OLYP), and J^3(OLYP), which predict $\Delta E(^4\Gamma - {}^2\Gamma)$ and $\Delta E(^6\Gamma - {}^2\Gamma)$ of ca. 10 000 and 26 000 cm^{-1}, respectively.

Table 4. Spin-State Energy Gaps for 1 and TpCoNO (1′, See Text) As Determined by DFT and *ab Initio* Computational Methods

	$\Delta E(^4\Gamma - {}^2\Gamma)/cm^{-1}$	$\Delta E(^6\Gamma - {}^2\Gamma)/cm^{-1}$
B3LYP, BS(3,2)[a]	9 440.4[d]	25 174.4[g]
	6 743.1[e]	17 981.6[h]
	8 079.5[f]	21 545.3[i]
OLYP, BS(3,2)[a]	12 770.6[d]	34 054.9[g]
	9 121.8[e]	24 324.8[h]
	10 117.1[f]	26 978.9[i]
CASSCF(5,5)	7 645.8	15 314.3
MR-DDCI3[b]	9 994.8	–
MR-DDCI3[c]	9 770.1	24 978.0
SORCI[b]	10 743.2	–
SORCI[c]	10 522.6	26 136.1

[a] DFT single-point energy calculations were performed on the OLYP-optimized geometry of **1**. [b] Multireference calculations were performed on top of the SA-CASSCF(5,5) calculations involving two roots corresponding to the ground states within the doublet and quartet spin manifolds. [c] Multireference calculations were performed on top of the SA-CASSCF(5,5) calculations involving three roots corresponding to the ground states within the doublet, quartet, and sextet spin manifolds. [d] Value equal to $-3J^1$. [e] Value equal to $-3J^2$. [f] Value equal to $-3J^3$. [g] Value equal to $-8J^1$. [h] Value equal to $-8J^2$. [i] Value equal to $-8J^3$.

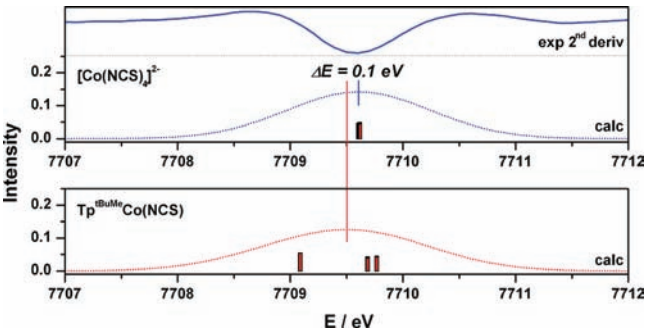

Figure 11. Comparison of the calculated initial pre-edge features of the Co K-edge XAS spectra of $[Co(NCS)_4]^{2-}$ (middle, blue dotted line) and $Tp^{tBu,Me}Co(NCS)$ (bottom, red dotted line), along with the second derivative of the experimental Co K-edge XAS spectrum of $[(Bu_4N)_2][Co(NCS)_4]$ (top, solid blue line).

TD-DFT Prediction of Co K-Edge XAS Spectra. Time-dependent DFT (TD-DFT) calculations employing the B3LYP functional provided excellent agreement between the calculated and experimental Co pre-K-edge XAS spectrum of $[Co(NCS)_4]^{2-}$

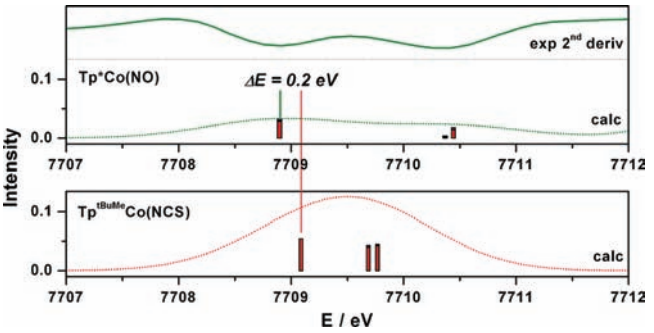

Figure 12. Comparison of the calculated initial pre-edge features of the Co K-edge XAS spectra of Tp*Co(NO) (middle, green dotted line) and $Tp^{tBu,Me}Co(NCS)$ (bottom, red dotted line), along with the second derivative of the experimental Co K-edge XAS spectrum of Tp*Co(NO) (top, solid green line).

Table 5. Experimental and Calculated Metric Parameters for Complexes 5 and 5′

	5^a	5^b	5^c	$5'^b$
Ni−NO (Å)	1.619(6)[d]	1.6180	1.6301	1.6169
	1.617(6)[e]			
N−O (Å)	1.170(7)[d]	1.1599	1.1720	1.1566
	1.158(7)[e]			
Ni−N Tp* (Å)	1.980(3)[d]	2.0407	2.0284	2.0477
	2.003(3)[e]			
	1.980(3)[d]	2.0420	2.0284	2.0477
	2.003(3)[e]			
	2.004(5)[d]	2.0420	2.0397	2.0488
	2.006(4)[e]			
Ni−N−O (deg)	178.5(6)[d]	180.0	176.6	179.4
	175.3(7)[e]			
α-angle (deg)	2.2[d]	0.1	2.7	0.4
	3.4[e]			

[a] Experimental data. [b] B3LYP-optimized data. [c] OLYP-optimized data. [d] Data for molecule 1 in the asymmetric unit. [e] Data for molecule 2 in the asymmetric unit.

(Figure 11). As expected, the intense pre-edge feature is predicted to result from β-spin excitations out of the Co 1s orbital and into the triply degenerate t_2 orbitals. The non-centrosymmetric coordination environment allows the formally Laporte-forbidden transition to gain intensity via 3d−4p mixing; the t_2 set in $[Co(NCS)_4]^{2-}$ is calculated to include ca. 8% Co 4p character per orbital.

By applying the energy correction needed for matching the calculated and experimental pre-edge features of the $[Co(NCS)_4]^{2-}$ spectra, we obtain excellent agreement between the experimental and calculated pre-edge transitions of **1** (Figure 11). The separation between the two observable features is well reproduced at ca. 1.5 eV, and the signals are predicted to arise from 1s excitation into the β-orbital of the SOMO at 7708.8 eV and into the $d_{xz/yz}$ NO-π^* antibonding combinations at 7710.4 eV (see Supporting Information).

We have also performed TD-DFT calculations on the structurally and electronically analogous complex $Tp^{tBu,Me}Co(NCS)$—an unambiguous example of high-spin Co(II) in a C_{3v}-symmetric N_4-ligand field.[92] In this case, the trigonal distortion splits the t_2 manifold into a lower-energy a_1 and a higher-energy e set (Figure 12), comprising the three unoccupied β-spin orbitals associated with the 1s→3d transitions shown in Figures 11 and 12. Assuming a fwhm of 1.5 eV, the spectrum displays a broad feature at 7709.5 eV, 0.1 eV lower in energy than the experimentally determined 1s→t_2 transitions for $[Co(NCS)_4]^{2-}$. Importantly, the calculated 7709.0 eV transition for $Tp^{tBu,Me}Co(NCS)$ closely matches with the initial spectral feature observed for **1** (7708.8 eV, ΔE = 0.2 eV, Figures 7 and 12). Both of these transitions are into largely metal-based molecular orbitals, and the small calculated energy difference between them again suggests a divalent metal center for **1**.

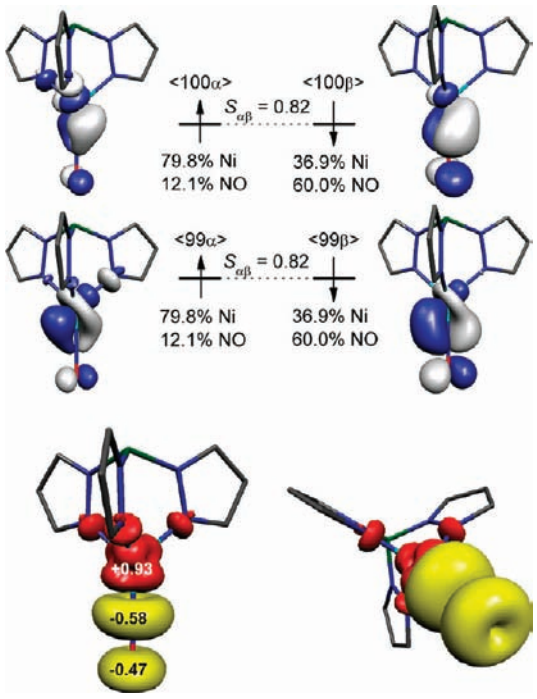

Figure 13. Calculated frontier UCOs (top) and spin density plots with numerically annotated Mulliken spin densities (bottom) of the B3LYP BS(2,2) ground state of **5**, using the RKS-B3LYP geometry-optimized coordinates. The methyl groups and hydrogens were removed for clarity. $S_{\alpha\beta}$ refers to the degree of spatial overlap between the magnetic orbitals.

DFT Calculations on Tp*Ni(NO). *Geometry Optimization and Ground-State Electronic Structure.* In light of the interest in describing the interaction between NO and late, first-row transition metals, we have extended our computational study to the related Ni complex Tp*Ni(NO) (**5**).[41,42] RKS-B3LYP and RKS-OLYP geometry optimization calculations both provided excellent agreement between the calculated and crystallographically determined molecular coordinates (Table 5).[42] The calculated and experimental α-angles are nearly 0° for **5**, consistent with predictions by Theopold and co-workers from extended Hückel and density functional theoretical calculations on related molecules.[95]

BS-B3LYP single-point energy calculations on the optimized coordinates resulted in BS(2,2) ground states, both lying ca. 4 kcal mol^{-1} lower in energy than the closed-shell solutions. The magnetic orbitals (Figure 13) are comprised of the metal-centered α-$d_{xz/yz}$ (79.8% Ni character) and ligand-centered β-NO-π^* (60.0% NO character) orbitals. While the spin density calculated by the BS-DFT methodology is not physically

Table 6. Spin-State Energy Gaps for 5 and TpNiNO (5′, See Text) As Determined by DFT and *ab Initio* Computational Methods

	$\Delta E(^3\Gamma - {}^1\Gamma)/cm^{-1}$	$\Delta E(^5\Gamma - {}^1\Gamma)/cm^{-1}$
B3LYP, BS(2,2)[a]	10 829.7[d]	32 489.1[g]
	7 219.8[e]	21 659.4[h]
	8 190.0[f]	24 570.0[i]
OLYP, BS(2,2)[a]	15 477.0[d]	46 431.0[g]
	10 318.0[e]	30 954.0[h]
	10 299.5[f]	30 898.5[i]
CASSCF(4,4)	10 626.6	18 880.8
MR-DDCI3[b]	12 478.9	–
MR-DDCI3[c]	12 721.5	31 941.9
SORCI[b]	13 509.9	–
SORCI[c]	13 147.9	32 156.4

[a] DFT single-point energy calculations were performed on the OLYP-optimized geometry of **5**. [b] Multireference calculations were performed on top of the SA-CASSCF(4,4) calculations involving two roots corresponding to the ground states within the singlet and triplet spin manifolds. [c] Multireference calculations were performed on top of the SA-CASSCF(4,4) calculations involving three roots corresponding to the ground states within the singlet, triplet, and quintet spin manifolds. [d] Value equal to $-2J^1$. [e] Value equal to $-2J^2$. [f] Value equal to $-2J^3$. [g] Value equal to $-6J^1$. [h] Value equal to $-6J^2$. [i] Value equal to $-6J^3$.

meaningful for singlet states, it can be interpreted as unpaired electron density and is thus useful for comparison with other complexes. The BS-B3LYP calculations predict spin density of +0.93 on Ni, −1.05 on NO, and +0.12 on the Tp* nitrogens (Figure 13). Considering the equal distribution of spin density in both the *x*- and *y*-components of the Ni−NO π^*-interaction,[16] this result is best described as an $S_{Ni} = 1$ Ni(II) center antiferromagnetically coupled to an $S_{NO} = 1$ NO^- anion.

OLYP single-point energy calculations on either of the optimized coordinates for **5** result in similar trends toward greater overlap in the magnetic orbitals as seen for **1**. The details are given in the Supporting Information, but the following points are notable: (i) the J^1(B3LYP), J^2(OLYP), and J^3(OLYP) values again provide the best agreement between the two functionals (Table 6) and (ii) the average $\Delta E(^3\Gamma - {}^1\Gamma)$ $(-2J)$ and $\Delta E(^5\Gamma - {}^1\Gamma)$ $(-6J)$ over these three *J*-values are ca. 10 500 and 31 500 cm^{-1}, respectively. These state energy splittings represent a modest increase from **1**, consistent with both the effect of the larger Z_{eff} for Ni vs Co on the energy of the d-manifold compared to the e-set of NO-π^* orbitals and the additional exchange stabilization available to the excited state of **1** and not **5**.

CASSCF/MRCI-Derived Ground-State Electronic Structures of TpM(NO) (M = Co, Ni). *Starting Geometries.* CASSCF/MRCI calculations were employed to more rigorously explore the ground-state electronic structures of complexes **1** and **5**. For both complexes a truncated form of the ligand was used in which the methyl groups on Tp* were exchanged for hydrogens (Tp). This modification is not expected to alter the qualitative results of this study due to the inactivity of the methyl groups in the valence electronic structure, and DFT(B3LYP) geometry optimization calculations on TpCo(NO) (**1′**) and TpNiNO (**5′**) provided metric parameters similar to those obtained for the Tp* complexes (Tables 3 and 5).

TpCo(NO). After screening various combinations of metal-d, NO-π, and NO-π^* orbitals, a 5-in-5 active space was chosen,

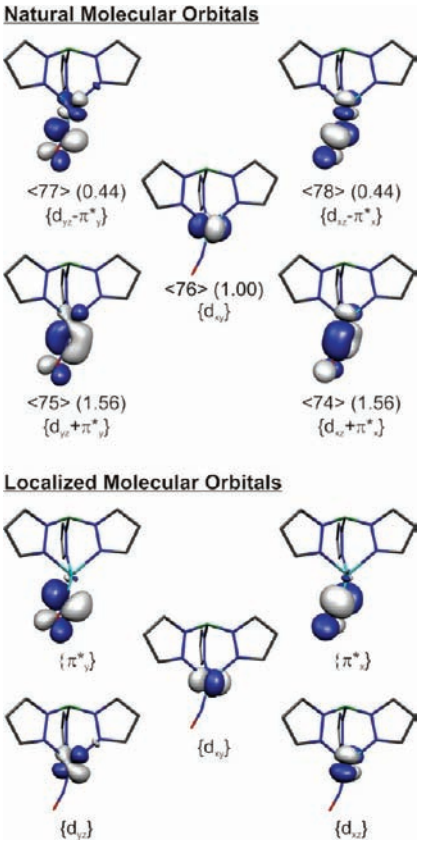

Figure 14. CAS orbitals for **1′** before (top) and after (bottom) Pipek−Mezey localization. The notation is as follow: <orbital number> (occupation) {valence bond description}.

which included the bonding and antibonding combinations of the Co-$d_{xz/yz}$ and NO-π^* orbitals as well as the metal-based SOMO (d_{xy}). Test calculations with larger active spaces, involving both Co-d_{z^2}/$d_{x^2-y^2}$ and ligand π orbitals, had little influence on the results. Optimization of the orbitals for the doublet state in the CASSCF(5,5) calculations yielded compositions very similar to those of the input orbitals. The lowest energy bonding (d+π^*) orbitals in the active space were composed of ca. 60% metal and 40% NO-π^* character; the SOMO was found to be 98% metal-based; and the two highest energy antibonding (d−π^*) orbitals were comprised of equal contributions from Co and NO-π^* orbitals (Figure 14). Thus, the interaction between the Co $d_{xy/yz}$ and NO-π^* orbitals can be described as having low ionicity, since the Co- and NO-based fragment orbitals contribute roughly equally to the bonding and antibonding combinations, but the small energy gap between the (d+π^*) and (d−π^*) orbitals of ca. 8 kcal mol^{-1} reflects the poor π-overlap between the fragment orbitals—as expected for a tetrahedral compound—indicating that admixture of configurations with formal single and double excitations into the (d−π^*) orbitals should figure significantly into the makeup of the ground state.

The principal configuration of the doublet, $^2\Phi_0 = |(d_{xz} + \pi^*_x)^2(d_{yz} + \pi^*_y)^2(d_{xy})^1(d_{yz} - \pi^*_y)^0(d_{xz} - \pi^*_x)^0\rangle$, accounts for 56.0% of the CAS wave function. None of the remaining configurations individually exceed 10% contribution; however, the three configurations resulting from formal double excitations out of $^2\Phi_0$ contribute 24.0% to the ground state. These latter configurations are comprised of the formal (d + π^*)-to-(d − π^*)

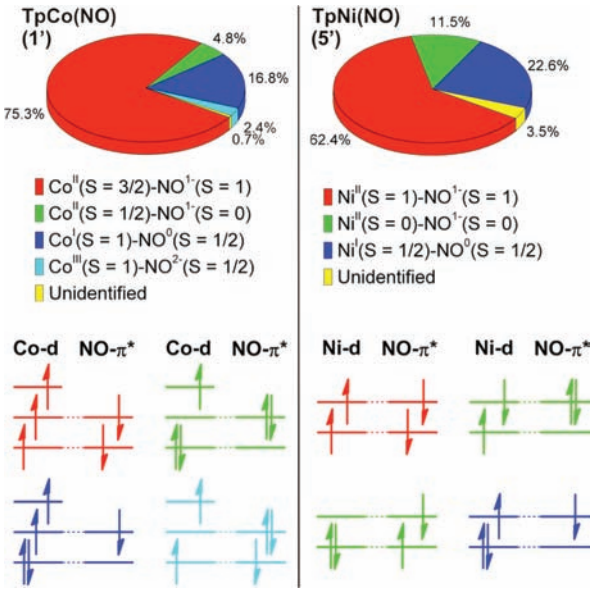

Figure 15. (Top) Analysis of the localized molecular orbital CAS wave functions for **1**′ (left) and **5**′ (right) in terms of M−NO resonance structures. (Bottom) Representative configurations for the individual valence bond oxidation state assignments.

excitations, and their significant admixture indicates that static correlation is important for describing the Co−NO π-bonding interaction, which may be interpreted (or equivalently described) as an antiferromagnetic coupling interaction between Co- and NO-based electrons.

To gain a better understanding of the valence bond picture represented by the CASSCF results, we performed a Pipek−Mezey localization of the active space orbitals. The CAS wave function in terms of the localized orbitals is identical to the CAS wave function given in terms of the state-averaged natural orbitals, but the localized orbitals may be interpreted more readily for the degree to which various distributions of electron density (valence bond pictures) contribute to the ground state. We note that a similar methodology has been used recently for providing detailed insight into the nature of related complexes as a means of understanding the interaction between biologically relevant metals and redox-active ligands.[24,96−98] In the present case, the localization procedure resulted in three d- and two NO-π^* orbitals as shown in Figure 14. From analysis of the resulting multireference state, we find that the antiferromagnetically coupled $S = {}^3/_2$ Co(II)/$S = 1$ NO^- configuration accounts for 75.3% of the ground state.[99] A further 4.8% of the ground state results from $S = {}^1/_2$ Co(II)/$S = 0$ NO^-, and 16.8% is contributed by $S = 1$ Co(I)/$S = {}^1/_2$ NO^0 configurations (Figure 15). The modest contributions from Co(I) resonance structures are consistent with the calculated and observed Co pre-K-edge XAS features, which indicated partial Co(I) character in the ground state. However, the localization procedure allows for a detailed assignment of the molecular electron density and thereby provides a clear indication that both **1** and **1**′ are best described as Co(II)/NO^- species.

Multireference configuration interaction calculations were performed as a means for evaluating both the quality of the active space for providing a reasonable zeroth-order wave function from CASSCF(5,5) calculations and for the influence of dynamic correlation effects on the calculated coupling parameters

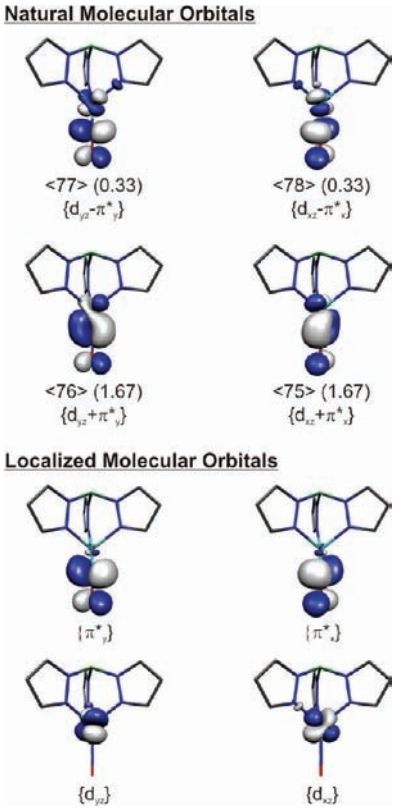

Figure 16. CAS orbitals for **5**′ before (top) and after (bottom) Pipek−Mezey localization. The notation is as follows: <orbital number> (occupation) {valence bond description}.

and energy ladder. The consistency of each BS calculation was also checked by comparing the DFT-derived doublet−quartet and doublet−sextet energy gaps to those obtained from CASSCF and MRCI calculations. The 5-in-5 reference space was found to adequately account for the majority of configurations contributing to the ground state (total weight of the reference space configurations in the final MRCI wave function >89% for $T_{sel} = 10^{-8}$ E_h) as determined by both the MR-DDCI3 and SORCI methods, and no configurations involving orbitals outside of the reference contributed more than 0.3% to the ground state. With tightening selection thresholds, the MRCI calculations converged across a range of methods and multiplicities to a doublet−quartet gap of ca. 10 000 cm^{-1} and a doublet−sextet gap of ca. 26 000 cm^{-1} (Table 4; for further details see the Supporting Information). When compared to the DFT results, these values correspond best with those derived from the three J-values mentioned above, found to provide the best agreement between the B3LYP and OLYP functionals: J^1(B3LYP), J^2(OLYP), and J^3(OLYP).

TpNi(NO). DFT calculations revealed that the experimentally observed C_{3v} symmetry of **5** resulted in a nonbonding d_{xy} orbital at lower energy than the $\{d_{xz/yz} + \pi^*_{x/y}\}$ bonding combinations. As a result, inclusion of the d_{xy} orbital in the active space of **5**′ had a negligible effect on the calculated wave function composition and energy ladder. Having tested larger active spaces involving all d orbitals and NO-π and -π^* orbitals, we arrived at a 4-in-4 active space which included the metal $d_{xz/yz}$ and NO-π^* orbitals. This active space provided a reasonable zeroth-order description of the ground states within each spin manifold under consideration. As with the TpCo(NO) CASSCF calculations, the $\{d + \pi^*\}$

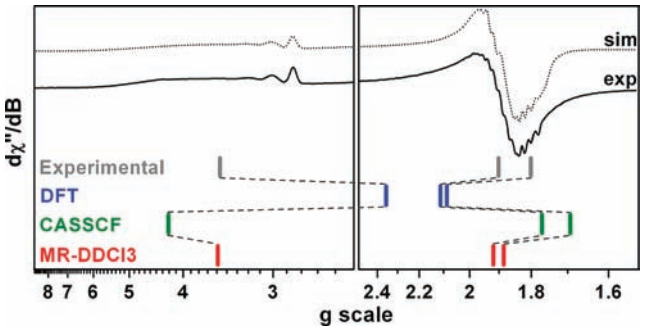

Figure 17. Comparison of experimental and calculated molecular *g*-values.

bonding combinations were each composed of 60% Ni and 40% NO-π^* character, and the $\{d - \pi^*\}$ antibonding combinations were nearly equal mixtures of Ni and NO-π^* character (48% and 50%, respectively; Figure 16). The contribution of the closed-shell configuration, $^1\Phi_0 = |(d_{xz} + \pi^*_x)^2(d_{yz} + \pi^*_y)^2(d_{yz} - \pi^*_y)^0(d_{xz} - \pi^*_x)^0\rangle$, to the singlet ground state increased to 71.2% compared to the analogous contribution of $^2\Phi_0$ to the ground state of **1′**, but the sum of the contributions from formally doubly excited configurations remained at 24.0%, suggesting a similar importance of static correlation in the metal−NO bond of **5′**.

Localization of the CA orbitals led to two metal-centered and two NO-π^* orbitals (Figure 16). Evaluation of the resulting MRCI wave function yielded a valence bond picture similar to that observed for **1′**, whereby an antiferromagnetic coupling configuration dominated the ground state, contributing 62.3% of the whole. A further 11.5% of the ground state was represented by more ionic Ni(II) configurations in which double excitation from one or both of the metal-based orbitals into both or one, respectively, of the NO-π^* orbitals led to an $S = 0$ Ni(II)/$S = 0$ NO^- configuration (Figure 15). Ni(I)−NO^0 configurations contributed a further 22.6% to the ground state, but, all together, the Ni(II) configurations accounted for 73.8%, allowing us to characterize complexes **5** and **5′** as Ni(II)-containing species with modest contributions from Ni(I) resonance structures. Importantly, the Ni(I) and Ni(II) configurations in this 4-in-4 reference space accounted for 96.5% of the ground state, indicating that any contributions from Ni(III) or Ni(IV) resonance structures are negligible at best.

The MR-DDCI3 and SORCI computational data for **5′** indicated that the 4-in-4 active space used for generating the SA-CASSCF orbitals adequately accounts for the majority (>87%) of the configurations contributing to the ground state (see Supporting Information). In this case, the MRCI calculations converged on singlet−triplet and singlet−quintet energy gaps of ca. 13 000 and 32 000 cm^{-1}, respectively (Table 6). As seen for **1**/**1′**, these results correlate well with those obtained by BS DFT, with the best agreement again being provided by the J^1(B3LYP), J^2(OLYP), and J^3(OLYP) coupling constants.

DFT, SA-CASSCF, and SA-CASSCF/MRCI Analysis of the Molecular *g*-Values for 1 and 1′. As stated above, the multireference character of the ground state of **1** may only be qualitatively reproduced by the single-determinant methods of DFT. Thus, while DFT was found to adequately reproduce the ground-state valence bond picture of this multireference system, it is ill-equipped to handle the calculation of relevant d−d multiplets, as would be needed for accurately predicting the

Table 7. Experimental and Calculated *g*-Values for 1 and 1′ [a]

	1		1′	
	expt	DFT	SA-CASSCF	MR-DDCI3
g_1	1.814	2.099	1.700	1.894
g_2	1.910	2.126	1.772	1.927
g_3	3.505	2.376	4.264	3.522

[a] See Experimental Section for computational details. MR-DDCI3 calculations were performed with $T_{sel} = 10^{-6}$ E_h.

EPR *g*-values of **1**. More precisely, the calculation of molecular *g*-tensors in DFT is based on linear response theory, which, with respect to SOC, is equivalent to first-order perturbation theory. As such, the linear response treatment is valid only when SOC effects are small, rendering it ineffective for modeling systems with low-lying d−d multiplets for which SOC contributions will be significant. The large deviations of the experimental *g*-values of **1** from the free-electron *g*-value are indicative of the presence of low-lying d−d multiplets, and, as one can see from Figure 17 and Table 7, the DFT-calculated *g*-tensor shows very poor agreement with the experimental data, predicting only modest deviations from the free-electron *g*-value. This discrepancy can be attributed to both inherent errors within DFT and the linear response formalism mentioned above.

To address this problem, we have performed a QDPT treatment of the SOC on the basis of all relevant multiplets arising from the distribution of nine electrons in both the five d orbitals and the two NO-π^* orbitals. Well-converged results were obtained by taking into account 20 roots within the spin doublet manifold. These states involve all excited multiplets which fall within approximately 30 000 cm^{-1} of the ground state, as obtained from the SA-CASSCF(9,7) and corresponding MRCI calculations. The inclusion of larger numbers of roots as well as the quartet and sextet states in the QDPT treatment had negligible effects on the calculated *g*-values. Prior to the inclusion of dynamic correlation effects, the SA-CASSCF(9,7) calculations already provided more realistic *g*-values than those obtained from DFT calculations (Figure 17, Table 7). In good qualitative agreement with the experimental data, the SA-CASSCF(9,7) treatment predicted a quasi-axial *g*-tensor with large anisotropy along the *z*-axis ($g_1 = 1.700$, $g_2 = 1.772$, and $g_3 = 4.264$). Careful examination of this result revealed that such a large deviation from the free-electron *g*-value is mainly due to the SOC-induced admixture of ∼10% of the first excited d−d multiplet, which arises at ∼1100 cm^{-1} and features leading configurations corresponding to the Co-$d_{x^2-y^2}/d_{z^2} \rightarrow$Co-$d_{xy}/d_{yz}$ transitions relative to the ground state. This leads to a large contribution of angular momentum to the *g*-tensor and thus accounts for its significant anisotropy.

As expected on the basis of simple perturbation theory considerations, the lowest-lying d−d multiplets will most efficiently mix with the ground state via SOC. As such, accurate calculations of the *g*-tensor require *quantitatively* correct predictions of the energy ladder and wave function compositions corresponding to the low-lying multiplets, and, indeed, improvements in the electronic structure description obtained upon inclusion of dynamic correlation effects via the MR-DDCI3 treatment led to quantitative agreement between the calculated and experimental *g*-values (Figure 17, Table 7). These calculations predict the first excited d−d multiplet to be at a noticeably

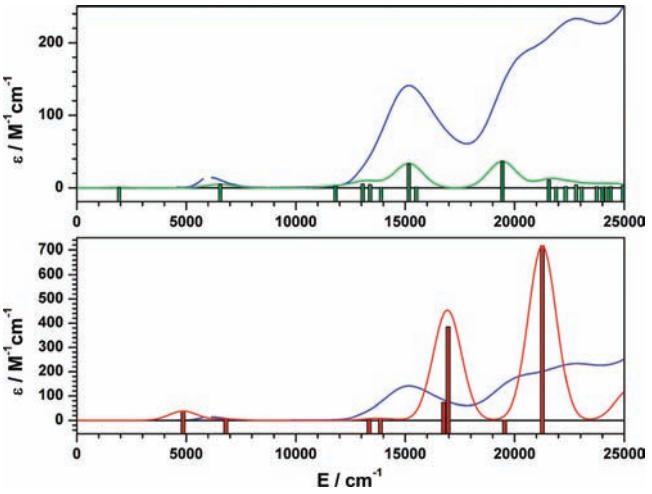

Figure 18. (Top) Comparison of the experimental (blue) and MR-DDCI3-calculated (green) vis−NIR spectra for **1** and **1′**, respectively. The MR-DDCI3-calculated spectrum was obtained using the 20-root SA-CASSCF(9,7) reference space described in the text. (Bottom) Comparison of the experimental (blue) and TD-DFT-calculated (red) vis−NIR spectra for **1**. In both plots, the vertical sticks represent individual transitions, and the vertical axis has been extended downward to better illustrate the positions of these transitions.

higher transition energy (∼2000 cm^{-1}) compared to the SA-CASSCF results. This shift reduces the SOC interaction to an admixture of ∼4% of the first excited d−d multiplet into the ground state, thus providing a quantitatively correct orbital angular momentum contribution to the *g*-tensor.

The accuracy of the calculated energy ladder corresponding to these states was also tested by comparison with the experimental absorption spectrum. The MR-DDCI3-calculated vis−NIR transitions obtained using the above-mentioned 20-root SA-CASSCF(9,7) reference are shown in Figure 18. The calculated transitions at 6549, 15 127, and 19 477 cm^{-1} define the general features of the calculated spectrum and well reproduce those found experimentally. The discrepancy between the experimental and calculated intensities is likely due to unaccounted-for vibrationally induced transition moments in the calculations, an omission that is not expected to significantly affect the predicted energy of the transitions. We also note a broad feature in the experimental IR spectrum of **1** (see Supporting Information) centered at ca. 2200 cm^{-1}, which may correspond to the lowest energy calculated transition, described above as occurring at ∼2000 cm^{-1}. For comparison, Figure 18 also shows the TD-DFT-calculated vis−NIR spectrum for **1′**. While TD-DFT predicts a similar number of transitions as MR-DDCI3 within this energy range, the agreement between the position of these features and the experimental spectrum differs by as much as 3000 cm^{-1}—a generally acceptable error, but clearly worse than the MR-DDCI3 calculations. The difference becomes particularly apparent in the lowest energy feature, for which TD-DFT predicts a transition at 4860 cm^{-1}. Running QDPT-SOC calculations with a manually adjusted diagonal energy for the first transition of 5000 cm^{-1} results in calculated *g*-values of g_1 = 2.055, g_2 = 2.091, and g_3 = 2.642, qualitatively identical to those obtained by DFT. Thus, overestimation of the first transition energy within DFT appears to be the primary mechanism responsible for the inability of the linear response DFT treatment to correctly model the *g*-tensor for **1**.

Here, we would note that although there is *qualitative* agreement between the results from the QDPT-SOC calculations with a manually adjusted diagonal energy for the first transition and the DFT calculations, the quantitative difference is nevertheless significant (g_3 = 2.642 for QDPT versus g_3 = 2.376 for DFT), suggesting that the inherent deficiencies of the first-order perturbation treatment of the linear response DFT, together with the single-reference approximation, also contribute to the deviation of the DFT results. However, due to technical reasons, the latter two factors cannot be separated from one another in our analysis.

DISCUSSION

Tp*Co(NO) (1) and Tp*Ni(NO) (5). The results of experimental work on **1** and DFT, CASSCF, and MRCI calculations on **1**/**1′** and **5**/**5′** resulted in a consistent valence bond picture for the two metal complexes: that of a high-spin M(II) (S_{Co} = $^3/_2$, S_{Ni} = 1) antiferromagnetically coupled to high-spin NO^- (S_{NO} = 1). Of the experimental data, the Co K-edge XAS results were particularly important, as the presence of two 1s→3d pre-edge features provided multiple means for comparing these data with both the XAS data of related complexes and those calculated by TD-DFT. The spectral features saddled the 1s→3d transition for $[Co^{II}(NCS)_4]^{2-}$—a trend that was well reproduced by TD-DFT calculations of the core-to-valence transition energies. The calculated XAS spectrum of $Tp^{tBu,Me}Co(NCS)$ predicted a similar splitting of the valence holes, the origin of which was tracked to the trigonal distortion imposed by the constrained geometry of the Tp^R ligands. The small energy difference between the initial 1s→3d transitions of $Tp^{tBu,Me}Co(NCS)$ (calculated) and **1** and the similarity of the calculated spectrum of $Tp^{tBu,Me}Co(NCS)$ to the calculated and experimental spectra of $[Co^{II}(NCS)_4]^{2-}$ provide a strong argument for assigning a +2 oxidation state to the metal center in **1**.

The X-band EPR data, consistent with a Co-centered, S_{tot} = $^1/_2$ spin system, were also of great importance for assigning the ground-state electronic structure of **1**. Both DFT and CASSCF calculations predicted a metal-based SOMO in the d_{xy} orbital—an orbital that is nonbonding in an idealized C_{3v} ligand field but gains antibonding character with the Tp* ligand as the NO group distorts away from the Co−B vector. The significant *g*-anisotropy observed experimentally was modeled with increasing accuracy as the effects of both static and dynamic correlation were taken into account and as SOC effects were treated up to an infinite order within perturbation theory. Thus, the linear-response methodology within DFT performed poorly, but QDPT treatment of the SOC, in conjunction with MRCI calculations, allowed for considerably more accurate assessment of contributions from d−d multiplets. These latter calculations suggested ca. 4% admixture via SOC of the first singlet excited state, itself predicted to have a transition energy of ∼2200 cm^{-1}. The excellent correlation between the calculated and observed vis−NIR transition energies lent support to the assignment of a broad feature in the IR spectrum at ∼2000 cm^{-1} to a low-energy d−d multiplet, itself calculated to be responsible for the majority of the anisotropy in the molecular *g*-tensor.

For both complexes, the spin contamination found by DFT—a common indicator of low-lying excited states—was found to be highly functional-dependent and tracked with their percent incorporation of HF theory. The hybrid functional B3LYP (20% HF) predicted considerable spin density on both the metal

and NO centers, while the GGA functional OLYP (0% HF) indicated a preference for electron delocalization. Interestingly, both the spin density profile (for **1**) and the J^3-based energy ladder predicted by the OLYP functional provided the best correlation with the MRCI results. Perhaps more important than the exact agreement between the *ab initio*- and DFT-predicted spin-state energy splittings, however, is the satisfactory replication by the MRCI methods of the *trend* in energy differences between various spin states for the Co and Ni complexes when compared to a simple *J*-based energy ladder scheme derived from the interaction of two distinct spin systems—$S = {}^3/_2$ $S = 1$ for Co and $S = 1$:$S = 1$ for Ni. Both the SORCI and MR-DDCI3 computational approaches predict ${}^{6(5)}\Gamma - {}^{2(1)}\Gamma$ energy gaps to be roughly 2.5 times the magnitude of the ${}^{4(3)}\Gamma - {}^{2(1)}\Gamma$ gaps for Co(Ni), well within the anticipated error of these calculations of ca. 2000 cm^{-1} and close to the predicted *J*-value-based ratios of 2.67 for Co and 3.00 for Ni.

Next, we note that the Ni(II)/NO^- valence bond structure for **5** contrasts markedly with (i) the traditional Ni(0)/NO^+ formulation[41] assumed for linear nitrosyl ligands and (ii) the recently proposed Ni(IV)/NO^{3-} formulation.[42] Since the amassed data for compound **1** clearly indicate a Co(II) oxidation state, the higher N−O stretching frequency for **5** (1786 cm^{-1}) compared to **1** (1732 cm^{-1}) argues against a Ni(IV)/NO^{3-} formulation. The origin of the increased N−O stretching frequency can be rationalized via several possible mechanisms. In terms of single-configurational ligand field theory, a change in the metal identity from Co to Ni would traditionally be thought to lead to an increase in the overlap between the metal d_π and NO_{π^*} orbitals of an NO^- anion, resulting in the transfer of electron density *out* of the NO π^* system and an increase in the N−O stretching frequency. This analysis, while tracking the experimental trend of ν_{NO}, does not, however, provide an explanation for the *majority contributions from the metal* in the bonding combinations of the d_π and NO_{π^*} orbitals of complexes **1** and **5** (see Figures 9 and 13). For this, the effect of the multireference character of the wave function must be considered, and the breakdown of the CAS wave function by valence bond structure in Figure 15 is particularly helpful. The greater percent contributions from M(I)/NO^0 configurations to the ground state of **5** relative to **1** would suggest greater NO^0 character for **5** over **1**, consistent with a higher NO stretching frequency for the Ni species.

Tp′Cu(NO). The computational results for **1** and **5** beg comparison with the more thoroughly studied Cu compounds Tp′Cu(NO) (Tp′ = $Tp^{tBu,H}$, $Tp^{tBu,iPr}$, $Tp^{Ph,Ph}$). The differences in the electronic structures of four-coordinate $\{MNO\}^{9/10/11}$ complexes could have important implications for understanding the structure and reactivity of the metal centers within Cu nitrite reductase (CuNIR) enzymes. While CuNIR is able to act as an NO reductase under anaerobic conditions via a mechanism believed to involve $\{CuNO\}^{11}$, the aerobic processing of nitrite likely involves a $\{CuNO\}^{10}$ species late in the catalytic cycle. It is interesting to note that a Cu(I)/$NO^\bullet$ formulation has been firmly established for the Tp′Cu(NO) complexes, but they all exhibit similar, if slightly lower, ν_{NO} (ca. 1700 cm^{-1}) compared to the Co and Ni analogues. In the course of our studies we have verified that our computational methodology used for **1**/**1**′ and **5**/**5**′ provides results in qualitative (and near quantitative) agreement (see Supporting Information) with those reported previously for both the Tp′CuNO and closely analogous complexes.

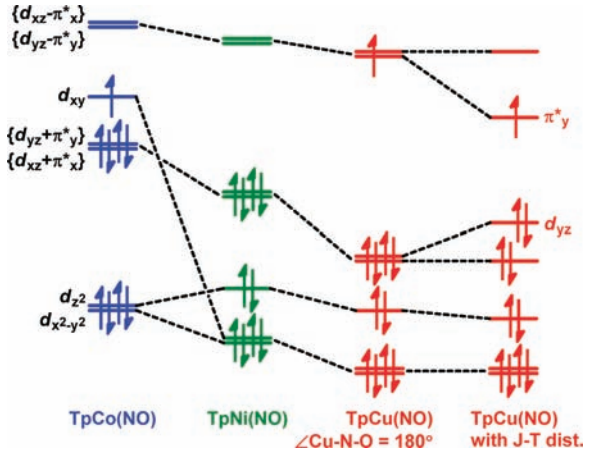

Figure 19. Qualitative MO scheme depicting the ordering of the frontier molecular orbitals for TpM(NO) (M = Co, Ni, Cu). The J-T distortion for TpCu(NO) involves bending the Cu−N−O angle to the experimentally determined value of 163°.

The distortion that gives rise to the nonlinear Cu−N−O bonding angle was shown by Lehnert and co-workers to heavily influence the calculated $g_\parallel$ value. This distortion can be thought to arise from the action of a J-T effect on the ^2E state of a hypothetical species with linear B−Cu−N and Cu−N−O bond angles (Figure 19). The net result can be visualized as the localization of the SOMO and HOMO onto the NO-π^*_y and Cu-d_{yz} orbitals, respectively, which accounts for the decrease in the calculated *g*-anisotropy with decreasing Cu−N−O angles. The combination of this J-T-induced orbital localization with the action of the larger Z_{eff} for Cu on its valence orbitals (Cu-d accounts for ca. 70% of $\{d_{xz} + \pi^*_x\}$) results in a clear d^{10} Cu(I) formulation with an NO^0 ($S = {}^1/_2$) ligand, as indicated by the experimentally determined EPR values of $g_\perp = 1.99$, $g_\parallel = 1.83$, $A_\perp^{Cu} = 62 \times 10^{-4}$ cm^{-1}, $A_\parallel^{Cu} = 107 \times 10^{-4}$ cm^{-1}, and $A_\perp^{N} = 27 \times 10^{-4}$ cm^{-1}.[39]

The multiconfigurational character of TpCuNO was evidenced by the relatively low contribution (∼80%) of the leading ground-state configuration, $^2\Phi_0 = |(d_{xz} + \pi^*_x)^2(d_{yz})^2(\pi^*_y)^1(d_{xz} - \pi^*_x)^0\rangle$, similar to the results originally reported by Cramer, Tolman, and co-workers from full CISD calculations on the model complex $[(H_3N)_3Cu(NO)]^+$; however, MR-DDCI3 calculations on the TpCuNO model compound (see Supporting Information) found only a 5% contribution to the ground state from the doubly excited configuration, $^2\Phi_1 = |(d_{xz} + \pi^*_x)^0(d_{yz})^2(\pi^*_y)^1(d_{xz} - \pi^*_x)\rangle$, indicating little static correlation in the bonding between the d_{xz} and π^*_x orbitals. Generally speaking, this multireference description, as well as the modest covalency in this system, leads to lower natural orbital occupation numbers than one might expect for a d^{10} configuration, but the polarization in the bonding combination toward Cu is consistent with a π-backbonding interaction with the NO-π^* orbital located in the *xz*-plane. Thus, the J-T-induced orbital localization in the *yz*-plane and the orbital polarization toward the metal in the *xz*-plane account for the similarity between the ν_{NO} for the Co, Ni, and Cu complexes, as all three species retain similar NO-based electron densities, albeit via different mechanisms.

This difference becomes particularly apparent upon inspection of the spin density plots for TpCu(NO) (Figure 20, Supporting Information). The orbital localization in the *yz*-plane is clear from the p_y orbital character of the spin density on the NO ligand,

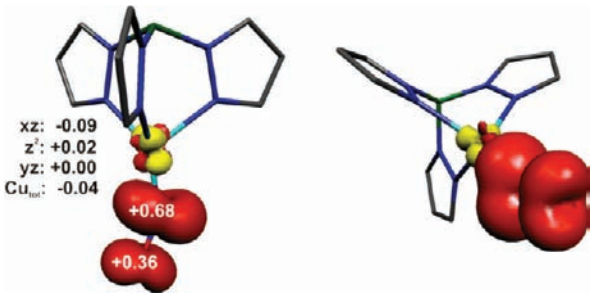

Figure 20. Spin density plots with numerically annotated Mulliken spin densities for TpCu(NO) from a single-point CASSCF(5,4) energy calculation.

suggesting very little bonding between the NO and the metal in this direction. In the *xz*-plane, the static correlation is evidenced by the antiferromagnetic coupling interaction of NO- and Cu-based electron densities. Thus, while **1** and **5** are both predicted to have two bonding interactions between the metal and NO, the bond order for TpCu(NO) should be closer to that of a single bond, consistent with the long experimental Cu−N_{NO} bond distance and the low thermal stability of Tp′Cu(NO) complexes with respect to NO dissociation.

SUMMARY AND CONCLUSIONS

The study of Tp*Co(NO) by multiple spectroscopic methods resulted in a ground-state electronic structure assignment comprising high-spin Co(II) (S_{Co} = $^3/_2$) antiferromagnetically coupled to a triplet NO^- (S_{NO} = 1). These results were informed by DFT and TD-DFT computational studies that performed well for predicting both the geometry of the complex and the spectroscopic features in XAS. However, the intrinsic shortcomings of DFT, including (i) its inability to properly account for the multireference character of both the ground-state and low-energy ligand field excitations and (ii) its inaccurate prediction of the corresponding energy ladder, led to very poor prediction of the considerable *g*-anisotropy of the EPR spectrum of **1**. In addition, for such a large deviation of the *g*-tensor from the free-electron value, the linear response formalism for treating SOC in the *g*-factor calculations was inappropriate. Thus, the combination of MRCI methods with the QDPT treatment of SOC was required for providing a quantitative model of the molecular *g*-tensor. The calculated lowest-lying ligand field transition at ∼2000 cm^{-1}, which was found to be responsible for the pronounced anisotropy of the *g*-tensor, was identified in the experimental IR spectrum of **1**. The DFT error in calculating the *g*-tensor was correlated with the error in the excitation energy for the lowest-lying d−d multiplet predicted by TD-DFT.

Beyond the specifics of the Co complex, the data presented above provide a coherent view of the bonding between NO and late, first-row transition metals in an otherwise trigonal, σ-donor environment. The geometric changes between the complexes—the α-angle as well as the M−N_{NO} and the N−O bond distances—and the variable bond dissociation energies were found to result from changes in the electron counts within the M−NO π-system: $\{CoNO\}^9$, $\{NiNO\}^{10}$, and $\{CuNO\}^{11}$. Thus, while the Feltham−Enemark notation is useful in this case for a self-contained set of molecules, the knowledge gained from this series would undoubtedly break down if applied to complexes with different geometries/coordination numbers. Furthermore, we find few changes between the Co and Ni complexes within this series. The additional electron on **5** enters a largely metal-based, nonbonding orbital, and any perturbation from the change in Z_{eff} is insubstantial with respect to the qualitative description of the ground state. For the Cu complex, the effect of populating one of the d_π−NO_{π^*} antibonding orbitals results in a J-T distortion, which manifests as a canting of oxygen away from the B−Cu−N_{NO} vector. Perhaps most significantly, this work suggests that formation of a $\{CuNO\}^{10}$ species in a similar coordination environment would exhibit (i) a linear B−Cu−N−O geometry, (ii) an increased N−O IR stretching frequency, and (iii) a significantly increased Cu−N_{NO} bond strength with respect to the analogous $\{CuNO\}^{11}$ species.

Finally, we point out that the overall S = $^1/_2$ Co complex **1** demonstrates the ability to bind an additional molecule of NO, readily reacting in solution to form Tp*Co$(NO)_2$ (**3**). This reactivity was observed spectroscopically by NMR analysis of a solution of **1** maintained under an atmosphere of NO, which indicated that the dinitrosyl complex, while itself not isolable, has an S = 0 ground state. Further evidence for the formation of **3** was provided by formation of the dinitrosoalkane species **4** when **1** was treated with norbornene under an atmosphere of NO. The reversibility of NO binding to form a pentacoordinate complex is of interest, considering the noted thermal stability of both four-coordinate dinitrosyl cobalt complexes and their closely related and biologically relevant four-coordinate dinitrosyl iron analogues. These results hint at coordination number effects on the ability of NO to bind Co (and Fe), which may prove important for biological NO transport and delivery mechanisms. Studies on the importance of coordination number for the stability, reactivity, and electronic structure of four- and five-coordinate dinitrosyl cobalt complexes are underway in our laboratories and will be reported in due course.

ASSOCIATED CONTENT

Supporting Information. Additional spectroscopic and computational details for **1**, **1′**, **4**, **5**, **5′**, $Tp^{tBu,H}$Cu(NO), and TpCu(NO) as well as the crystallographic information file (CIF) for **1**. This material is available free of charge via the Internet at http://pubs.acs.org.

AUTHOR INFORMATION

Corresponding Author

rbergman@berkeley.edu; serena.debeer@cornell.edu, fdtoste@berkeley.edu; wieghardt@mpi-muelheim.mpg.de

ACKNOWLEDGMENT

N.C.T. thanks the Max-Planck-Gesellshaft for financial support; R.G.B. thanks the NSF for financial support in the form of a research grant (CHE-0841786); M.R.C. acknowledges the Royal Commission for the Exhibition of 1851 for the provision of a research fellowship; and S.D. thanks Cornell University for funding. This work has profited from discussions with Dr. Dmitry Ganyushin, Kantharuban Sivalingam, Dr. Thomas Weyhermüller, and Prof. Dr. Frank Neese. SSRL operations are funded by the Department of Energy, Office of Basic Energy Sciences. The Structural Molecular Biology program is supported by the National Institutes of Health (grant 5 P41RR001209), National Center for Research Resources, Biomedical Technology Program,

and the U.S. Department of Energy, Office of Biological Environmental Research.

REFERENCES

(1) *Nitric Oxide: Biology and Pathobiology*; Ignarro, L. J., Ed.; Academic Press: San Diego, CA, 2000.
(2) Moncada, S.; Palmer, R. M. J.; Higgs, E. A. *Pharmacol. Rev.* **1991**, *43*, 109.
(3) *Methods in Nitric Oxide Research*; Feelisch, M., Stamler, J. S., Eds.; John Wiley and Sons: Chichester, England, 1996.
(4) Wink, D. A.; Hanbauer, I.; Grisham, M. B.; Laval, F.; Nims, R. W.; Laval, J.; Cook, J.; Pacelli, R.; Liebmann, J.; Krishna, M.; Ford, P. C.; Mitchell, J. B. *Curr. Top. Cell. Regul.* **1996**, *34*, 159.
(5) Ford, P. C.; Fernandez, B. O.; Lim, M. D. *Chem. Rev.* **2005**, *105*, 2439.
(6) McCleverty, J. A. *Chem. Rev.* **2004**, *104*, 403.
(7) Mingos, D. M. P.; Sherman, D. J. *Adv. Inorg. Chem.* **1989**, *34*, 293.
(8) Richter-Addo, G. B.; Legzdins, P. *Metal Nitrosyls*; Oxford University Press: New York, 1992.
(9) Enemark, J. H.; Feltham, R. D. *Coord. Chem. Rev.* **1974**, *13*, 339.
(10) Wyllie, G. R. A.; Scheidt, W. R. *Chem. Rev.* **2002**, *102*, 1067.
(11) Ghosh, A. *Acc. Chem. Res.* **2005**, *38*, 943.
(12) Ghosh, A. J. *Biol. Inorg. Chem.* **2006**, *11*, 712.
(13) Radón, M.; Pierloot, K. *J. Phys. Chem. A* **2008**, *112*, 11824.
(14) Olah, J.; Harvey, J. N. *J. Phys. Chem. A* **2009**, *113*, 7338.
(15) Harrop, T. C.; Song, D.; Lippard, S. J. *J. Am. Chem. Soc.* **2006**, *128*, 3528.
(16) Conradie, J.; Quarless, D. A., Jr.; Hsu, H.-F.; Harrop, T. C.; Lippard, S. J.; Koch, S. A.; Ghosh, A. *J. Am. Chem. Soc.* **2007**, *129*, 10446.
(17) Ray, M.; Golombek, A. P.; Hendrich, M. P.; Yap, G. P. A.; Liable-Sands, L. M.; Rheingold, A. L.; Borovik, A. S. *Inorg. Chem.* **1999**, *38*, 3110.
(18) Franz, K.; Lippard, S. J. *J. Am. Chem. Soc.* **1999**, *121*, 10504.
(19) Tangen, E.; Conradie, J.; Ghosh, A. *Inorg. Chem.* **2005**, *44*, 3699.
(20) Conradie, J.; Ghosh, A. *J. Inorg. Biochem.* **2006**, *100*, 2069.
(21) Conradie, J.; Ghosh, A. *J. Phys. Chem. B.* **2007**, *111*, 12621.
(22) Hopmann, K. H.; Conradie, J.; Ghosh, A. *J. Phys. Chem. B.* **2009**, *113*, 10540.
(23) Wells, F. V.; McCann, S. W.; Wickman, H. H.; Kessel, S. L.; Hendrickson, D. N.; Feltham, R. D. *Inorg. Chem.* **1982**, *21*, 2306.
(24) Radón, M.; Broclawik, E.; Pierloot, K. *J. Phys. Chem. B.* **2010**, *114*, 1518.
(25) Aquino, F.; Rodriguez, J. H. *J. Phys. Chem. A* **2009**, *113*, 9150.
(26) Brown, C. A.; Pavlosky, M. A.; Westre, T. E.; Zhang, Y.; Hedman, B.; Hodgson, K. O.; Solomon, E. I. *J. Am. Chem. Soc.* **1995**, *117*, 715.
(27) Cheng, H.-Y.; Chang, S.; Tsai, P.-Y. *J. Phys. Chem. A* **2004**, *108*, 358.
(28) Li, M.; Bonnet, D.; Bill, E.; Neese, F.; Weyhermüller, T.; Blum, N.; Sellmann, D.; Wieghardt, K. *Inorg. Chem.* **2002**, *41*, 3444.
(29) Pohl, K.; Wieghardt, K.; Nuber, B.; Weiss, J. *J. Chem. Soc., Dalton Trans.* **1987**, 187.
(30) Rodriguez, J. H.; Xia, Y.-M.; Debrunner, P. G. *J. Am. Chem. Soc.* **1999**, *121*, 7846.
(31) Schlenk, G.; Pau, M. Y. M.; Solomon, E. I. *J. Am. Chem. Soc.* **2004**, *126*, 505.
(32) Serres, R. G.; Grapperhaus, C. A.; Bothe, E.; Bill, E.; Weyhermüller, T.; Neese, F.; Wieghardt, K. *J. Am. Chem. Soc.* **2004**, *126*, 5138.
(33) Zhang, Y.; Oldfield, E. *J. Am. Chem. Soc.* **2004**, *126*, 9494.
(34) Zhang, Y.; Pavlosky, M. A.; Brown, C. A.; Westre, T. E.; Hedman, B.; O., H. K.; Solomon, E. I. *J. Am. Chem. Soc.* **1992**, *114*, 9189.
(35) Goodrich, L. E.; Paulat, F.; Praneeth, V. K. K.; Lehnert, N. *Inorg. Chem.* **2010**, *49*, 6293–6316.
(36) Aquilante, F.; Malmqvist, P.; Pedersen, T. B.; Ghosh, A.; Roos, B. O. *J. Chem. Theory Comput.* **2008**, *4*, 694.
(37) Chen, H.; Lai, W.; Shaik, S. *J. Phys. Chem. B* **2011**, *115*, 1727.
(38) Carrier, S. M.; Ruggiero, C. E.; Tolman, W. B.; Jameson, G. B. *J. Am. Chem. Soc.* **1992**, *114*, 4407.
(39) Ruggiero, C. E.; Carrier, S. M.; Antholine, W. E.; Whittaker, J. W.; Cramer, C. J.; Tolman, W. B. *J. Am. Chem. Soc.* **1993**, *115*, 11285.
(40) Fujisawa, K.; Tateda, A.; Miyashita, Y.; Okamoto, K.; Paulat, F.; Praneeth, V. K. K.; Merkle, A.; Lehnert, N. *J. Am. Chem. Soc.* **2008**, *130*, 1205.
(41) Harding, D. J.; Harding, P.; Adams, H.; Tuntulani, T. *Inorg. Chim. Acta* **2007**, *360*, 3335.
(42) Landry, V. K.; Pang, K.; Quan, S. M.; Parkin, G. *Dalton Trans.* **2007**, 820.
(43) Gwost, D. G.; Caulton, K. C. *Inorg. Synth.* **1976**, *16*, 16.
(44) Gwost, D. G.; Caulton, K. G. *Inorg. Chem.* **1973**, *12*, 2095.
(45) Hanson, G. R.; Gates, K. E.; Noble, C. J.; Griffin, M.; Mitchell, A.; Benson, S. *J. Inorg. Biochem.* **2004**, *98*, 903.
(46) George, G. N. *EXAFSPAK*; Stanford Synchrotron Radiation Laboratory, Stanford Linear Accelerator Center, Stanford University: Stanford, CA, 1996.
(47) Tenderholt, A. *PySpline*; Stanford Synchrotron Radiation Laboratory; Stanford Linear Accelerator Center, Stanford University: Stanford, CA, 2005.
(48) Mustre de Leon, J.; Rehr, J. J.; Zabinsky, S. I.; Albers, R. C. *Phys. Rev. B* **1991**, *44*, 4146.
(49) Neese, F. *Orca—An Ab Initio, DFT, and Semiempirical Electronic Structure Package*, version 2.8; Institut für Physikalische und Theoretische Chemie, Universität Bonn: Bonn, Germany, 2010.
(50) Handy, N. C.; Cohen, A. J. *Mol. Phys.* **2001**, *99*, 403.
(51) Becke, A. D. *J. Chem. Phys.* **1993**, *98*, 5648.
(52) Lee, C. T.; Yang, W. T.; Parr, R. G. *Phys. Rev. B* **1988**, *37*, 785.
(53) Stephens, P. J.; Devlin, F. J.; Chabalowski, C. F.; Frisch, M. J. *J. Phys. Chem.* **1994**, *98*, 11623.
(54) Weigend, F.; Ahlrichs, R. *Phys. Chem. Chem. Phys.* **2005**, *7*, 3297.
(55) Kendall, R. A.; Dunning, T. H.; Harrison, R. J. *J. Chem. Phys.* **1992**, *96*, 6796.
(56) Neese, F.; Wennmohs, F.; Hansen, A.; Becker, U. *Chem. Phys.* **2009**, *356*, 98.
(57) Weigend, F. *Phys. Chem. Chem. Phys.* **2006**, *8*, 1057.
(58) Grimme, S. *J. Comput. Chem.* **2004**, *25*, 1463.
(59) Grimme, S. *J. Comput. Chem.* **2006**, *27*, 1787.
(60) Grimme, S.; Antony, J.; Ehrlich, S.; Krieg, H. *J. Chem. Phys.* **2010**, *132*, 154104.
(61) Neese, F. *J. Phys. Chem. Solids* **2004**, *65*, 781.
(62) Neese, F. *J. Am. Chem. Soc.* **2006**, *128*, 10213.
(63) *Molekel. Advanced Interactive 3D-Graphics for Molecular Sciences*, available at http://www.cscs.ch/molkel.
(64) Kirchner, B.; Wennmohs, F.; Ye, S.; Neese, F. *Curr. Opin. Chem. Biol.* **2007**, *11*, 134.
(65) DeBeer George, S.; Petrenko, T.; Neese, F. *Inorg. Chim. Acta* **2008**, *361*, 965.
(66) DeBeer George, S.; Petrenko, T.; Neese, F. *Phys. Chem. A* **2008**, *112*, 12936.
(67) Neese, F. *Inorg. Chim. Acta* **2002**, *337*, 181.
(68) Noodleman, L. *J. Chem. Phys.* **1981**, *74*, 5737.
(69) Noodleman, L.; Davidson, E. R. *Chem. Phys.* **1985**, *109*, 131.
(70) Ginsberg, A. P. *J. Am. Chem. Soc.* **1980**, *102*, 111.
(71) Bencini, A.; Gatteschi, D. *J. Am. Chem. Soc.* **1980**, *108*, 5763.
(72) Yamaguchi, K.; Takahara, Y.; Fueno, T. In *Applied Quantum Chemistry*; Smith, V. H., Schaefer, F., Morokuma, K., Eds.; D. Riedel: Dordrecht, The Netherlands, 1986; p 155.
(73) Soda, T.; Kitagawa, Y.; Onishi, T.; Takano, Y.; Shigeta, Y.; Nagao, H.; Yoshioka, Y.; Yamaguchi, K. *Chem. Phys. Lett.* **2000**, *319*, 223.
(74) Miralles, J.; Castell, O.; Caballol, R.; Malrieu, J. P. *Chem. Phys. Lett.* **1993**, *172*, 33.
(75) Neese, F. *J. Chem. Phys.* **2003**, *119*, 9428.
(76) Gerloch, M.; McMeeking, R. F. *J. Chem. Soc., Dalton Trans.* **1975**, 2443.
(77) Blovin, H. *ChemPhysChem* **2006**, *7*, 1575.
(78) Ganyushin, D.; Neese, F. *J. Chem. Phys.* **2006**, *125*, 024103/024101–024103/024111.

(79) Neese, F. *J. Chem. Phys.* **2005**, *122*, 034107.
(80) Thyagarajan, S.; Incarvito, C. D.; Rheingold, A. L.; Theopold, K. H. *Inorg. Chim. Acta* **2003**, *345*, 333.
(81) Crimmin, M. R.; Rosebrugh, L. E.; Tomson, N. C.; Weyhermüller, T.; Bergman, R. G.; Toste, F. D.; Wieghardt, K. *J. Organomet. Chem.* **2011**, doi 10.1016/j.jorganchem.2011.04.038.
(82) Detrich, J. L.; Reinaud, O. M.; Rheingold, A. L.; Theopold, K. H. *J. Am. Chem. Soc.* **1995**, *117*, 11745.
(83) Becker, P. N.; Bergman, R. G. *Organometallics* **1983**, *2*, 787.
(84) Becker, P. N.; Bergman, R. G. *J. Am. Chem. Soc.* **1983**, *105*, 2985.
(85) Becker, P. N.; White, M. A.; Bergman, R. G. *J. Am. Chem. Soc.* **1980**, *102*, 5676.
(86) Boyd, W. C.; Crimmin, M. R.; Rosebrugh, L. E.; Schomaker, J. M.; Bergman, R. G.; Toste, F. D. *J. Am. Chem. Soc.* **2010**, *132*, 16365.
(87) Brunner, H.; Loskot, S. *Angew. Chem., Int. Ed.* **1971**, *10*, 515.
(88) Brunner, H.; Loskot, S. *J. Organomet. Chem.* **1973**, *61*, 401.
(89) Evrard, G.; Thomas, R.; Davis, B. R.; Bernal, I. *J. Organomet. Chem.* **1977**, *124*, 59.
(90) Schomaker, J. M.; Boyd, W. C.; Stewart, I. C.; Toste, F. D.; Bergman, R. G. *J. Am. Chem. Soc.* **2008**, *130*, 3777.
(91) Multiple SQUID magnetometry measurements on **1** from independently prepared samples gave values for μ_{eff} ranging from 2.3 to 2.9 μ_B, higher than the expected value of 2.19 μ_B. A quantitative EPR experiment, using a known concentration of Cu^{2+} as a standard, indicated that the S = $^1/_2$ signal comprised the entirety of the sample (approximate error of 10%), suggesting that the high values observed are due to low molecular weight, highly paramagnetic impurities.
(92) Krzystek, J.; Swenson, D. C.; Zvyagin, S. A.; Smirnov, D.; Ozarowski, A.; Telser, J. *J. Am. Chem. Soc.* **2010**, *132*, 5241.
(93) Hopmann, K. H.; Noodleman, L.; Ghosh, A. *Chem.—Eur. J.* **2010**, *16*, 10397.
(94) Conradie, J.; Ghosh, A. *Inorg. Chem.* **2011**, *50*, 4223.
(95) Detrich, J. L.; Konečný, R.; Vetter, W. M.; Doren, D.; Rheingold, A. L.; Theopold, K. H. *J. Am. Chem. Soc.* **1996**, *118*, 1703–1712.
(96) Chen, H.; Ikeda-Saito, M.; Shaik, S. *J. Am. Chem. Soc.* **2008**, *130*, 14778–14790.
(97) Roos, B. O.; Veryazov, V.; Conradie, J.; Taylor, P. R.; Ghosh, A. *J. Phys. Chem. B* **2008**, *112*, 14099–14102.
(98) Pierloot, K.; Zhao, H.; Vancoillie, S. *Inorg. Chem.* **2010**, *49*, 10316–10329.
(99) For this and all subsequent assignments, we are assuming that on-site exchange dominates when determining the relative spin orientation of individual electrons, but the computational output provides only the total weight of all determinants corresponding to the same configuration. Thus, while the oxidation state assignments from these results are unambiguous, the specific spin state of the metal and NO fragments is presently unknown.